Hybrid Inkjet and Direct-Write Multi-Material Additive Manufacturing

by

Nicholas Graham Bandiera
B.Eng., McMaster University (2015)

Submitted to the Department of Mechanical Engineering
in Partial Fulfillment of the Requirements for the Degree of
Master of Science in Mechanical Engineering

at the

MASSACHUSETTS INSTITUTE OF TECHNOLOGY

June 2017

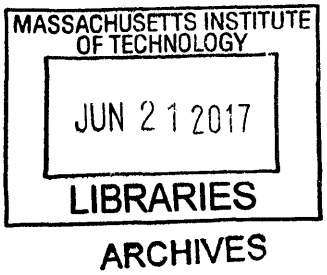

Author ..... Signature redacted
Department of Mechanical Engineering
May 12, 2017

Certified by ..... Signature redacted
Wojciech Matusik
Associate Professor of Electrical Engineering and Computer Science
Thesis Supervisor

Certified by ..... Signature redacted
A. John Hart
Associate Professor of Mechanical Engineering
Mechanical Engineering Faculty Reader

Accepted by ..... Signature redacted
Rohan Abeyaratne
Quentin Berg Professor of Mechanics
Chairman, Committee on Graduate Students

Hybrid Inkjet and Direct-Write Multi-Material Additive Manufacturing

by

Nicholas Graham Bandiera

Submitted to the Department of Mechanical Engineering
on May 12, 2017 in Partial Fulfillment of the
Requirements for the Degree of Master of Science in
Mechanical Engineering

ABSTRACT

Recently there has been a trend towards combining multiple forms of additive manufacturing together for increased functionality, freedom and efficiency. In this work, two forms of multiple-material additive manufacturing technologies – inkjet and direct-ink writing – are combined in a hybrid system. Several advantages are realized due to the increased material library and geometric freedom as a result of new printing modalities.

Initially, models of each process are reviewed and the processes are evaluated for compatibility. Then, the precision machine design of a passively-indexed, carousel-style, syringe tool holder is completed. An error budget employing Homogeneous Transformation Matrices was maintained to estimate the tooltip errors. In order to register these two non-contact printing processes, a unique approach to their registration to a common global origin was necessary. A single non-contact optical CCD micrometer is used to register the three spatial coordinates of the syringe tooltip. Measurements are performed to characterize the repeatability of the nozzle registration scheme and the constructed gantry and carousel system, which well exceeds the requirements and the predictions from the conservative error budget.

This novel system can print with a wide array of inks, including those that solidify via polymerization or crosslinking, two part chemistries, solvent evaporation or sintering, as well as liquids, gels and pastes. These materials can have a wide range of mechanical properties and functionalities, for example electrical conductivity or force sensitive resistivity.

Models for the extrudate flow rate are used alongside experimental determination of the extrudate cross-section to ensure accurate process congruence. Finally, printed results demonstrate the various printing techniques, highlight the expanded material library, and display novel assemblies not possible with conventional additive processes. One such example is a fully printed pressure sensor array.

Thesis Supervisor: Wojciech Matusik
Title: Associate Professor of Electrical Engineering and Computer Science

Mechanical Engineering Faculty Reader: A. John Hart
Title: Associate Professor of Mechanical Engineering

Acknowledgements

First and foremost, I would like to thank my parents, Brenda and Paul, for their unconditional support over the years. Thank you for always believing in me.

I would also like to thank my academic advisor, Professor Wojciech Matusik, for the opportunity to pursue research in 3D printing. Working with a fantastic group of people with such a breadth of backgrounds on an interdisciplinary project was a great experience. In particular, I would like to thank Alexandre Kaspar and Pitchaya Sitthi-Amorn for their exceptional work on G-code implementation and hardware integration, respectively. The work in this thesis would not have been possible without their coding expertise. Thanks also to Michael Foshey and Javier Ramos for the feedback on the mechanical aspects of the design and hardware debugging, David Kim for preparing all of the inks and help with fluid characterization, and to Bryt Bradley for her diligence in managing the numerous orders I placed for this project. A special thank you goes out to Subramanian Sundaram for the help with things in the electrical domain and the insightful discussions.

(this page intentionally left blank)

Contents

(this page intentionally left blank)

Figures

(this page intentionally left blank)

Tables

(this page intentionally left blank)

Chapter 1: Introduction

The purpose of this thesis is to present a novel combination of additive manufacturing (AM) processes for an increase in available material combinations and geometries. This work is important as with a wider range of materials and printing modes available, the designer has increased freedom. AM continues to find uses in creating intricate, complex and bespoke geometries.

1.1 Additive Manufacturing

Additive manufacturing can been seen the opposite of subtractive manufacturing. A part is created by the selective, layer-wise deposition of material as opposed to the selective removal of material from a piece of stock. Subtractive methods, while widespread in industry, suffer from several inherent limitations including the waste of the removed material, geometry limitations (such as undercuts or deep, complex internal features), as well as the need for tooling and setup, and the largely homogenous materials and material properties.

Additive manufacturing (AM) has opened a myriad of possibilities in terms of material combinations and geometries. Freeform geometries with spatially-varying material properties are but one example that highlights the flexibility of this process. Widespread adoption of AM has historically been hindered by its slower rate of production and higher cost when compared to conventional manufacturing technologies. To overcome these disadvantages, the parts made via AM must be high value-added, bespoke, remove complication from an existing design (ex. reducing the part count) or must benefit from the elimination of tooling [1].

1.2 Current AM Processes

Many different technologies have been developed which fit under the AM umbrella including, but not limited to, Laminated Object Manufacturing (LOM), MultiJet Printing (MJP), binder jetting (3D Printing[1][2]), material extrusion (ex. Fused Filament Deposition), vat photopolymerization (SLA or DLP SLA), powder bed technologies such as Selective Laser Sintering (SLS), Selective Laser Melting (SLM), and Selective Inhibition Sintering (SIS) or directed energy deposition. The reader is encouraged to read Additive Manufacturing Technologies [3] for a comprehensive review of existing technologies.

[1] 3D Printing is the official name for the inkjet binder and powder bed consolidation technique developed at MIT by Professors Sachs and Cima and licensed to ZCorp. Colloquially, it has come to encompass any digital additive manufacturing process. Any references to 3D printing hereafter will be taken as a synonym for AM.

Every process has its strengths and limitations. Recently, there has been a trend towards combining different additive (and sometimes, subtractive) processes together to create a more versatile machine [4] in so-called 'hybrid' processes. It is true that the chosen processes are often separable, however having them combined in a single machine eliminates the need for ferrying the workpiece to different workstations and can aid with process registration. Another approach is to shuttle the build tray between various stations in an automated fashion. Such combinations of processes ideally offer functionality greater than the sum of their constituents.

Another feature which differentiates additive processes from one another is the ability to make parts from multiple materials. Vaezi et al. reviewed multiple material additive manufacturing and concisely list its benefits: Design freedom, design protection, increased functionality, elimination of assembly, efficient manufacturing system [5]. There are three main levels of freedom associated with multiple material printing:

1. Materials can between layers
2. Materials can vary within layers
3. Materials can vary within and between layers

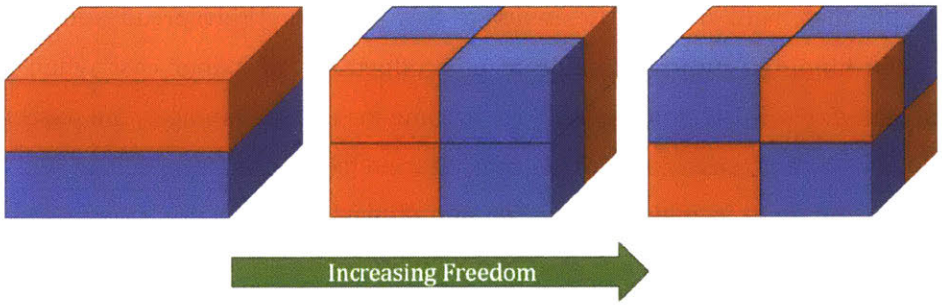

Figure 1.1: Simplified representation of multiple material additive manufacturing. Orange and blue are two different materials. Reproduced from [5].

Currently, the only technologies offering the full range of spatial material freedom are inkjet-based, or complicated customized DLP SLA processes with multiple material switches. Each of these technologies has the advantage of being a parallel process with the notion of a *vol*umetric pi*xel*, called a *voxel*. Many serial processes offer multiple materials through the use of multiple deposition heads, but do not offer the same level of spatial resolution.

Additive manufacturing is an extremely multi-disciplinary pursuit, involving aspects of machine design, mechatronics, process control, electrical engineering, materials engineering,

chemical engineering, and computation. All domains must work together closely to achieve a quality output.

1.3 Hybrid Systems

There exist several different hybrid printing machines in academia and others that have been commercialized. A list of all hybrid machines known to the author is presented below with some commentary. Combined additive and subtractive technologies are not considered here.

Table 1.1: Summary of existing hybrid additive technologies

Company/Group (Process Name)	Technologies	Use case and materials	Number of materials	Refer-ences
Voxel 8 (Multi-matieral Digital Manufacturing)	FDM + DW	Embedded electronics. Thermoplastic or epoxy and silver ink.	2 (Thermoplastic and conductive silver ink)	
Rize 3D (Augmented Polymer Deposition)	FDM + inkjet	Support removal from thermoplastic FDM parts, and marking ink	3	[6],[7]
PARC	Aerosol jet + inkjet + extruders	Printed electronics	Unknown	[8], [9]
MGI	Inkjet + aerojet	Printed electronics	8	[10]
University of Waterloo Multi-scale Additive Manufacturing Laboratory	Binder jet + micro-syringe deposition	Bioceramic scaffolds for bone	1 (after removing syringe-deposited support)	[11]
Collider	DLP SLA + Filling	Casting elastomers	1 (after removing soluble DLP mold)	[12]
Yale University	FDM + Filling	Increasing strength using epoxy, selective flexible linkages with elastomers	Multiple filling materials	[13]
W.M. Keck Center for 3D Innovation, The University of Texas	SLA + DW	Photopolyer and silver ink for printed electronics	2	[14]
Optomec, Inc	FDM + DW	Thermoplastic and silver ink, UV epoxy for printed electronics	3	[15]
Cornell University	FDM + Robocasting	Electromagnets, transistors, embedded sensors	Multiple	[16],[17]

Many of the reported hybrid technologies may not be complete, automated systems but rather exist as two distinct machines. The hybrid printer developed in this work leverages the custom hardware developed by the Computational Fabrication Group at MIT as part of the MultiFab project which enables multi-material deposition. Details on the hardware development can be found in various theses [18]–[20].

1.3.1 Motivation

There exists a void in the current AM landscape for the embedding of functional structures within a multiple material print. The multiple material direct-write system augments the capabilities of the multiple material inkjet system.

1.4 Thesis Outline and Summary

The motivation behind this work and an overview of similar technologies have been discussed in the first chapter. Chapter 2: Background discusses process fundamentals and explains the selection of the time-pressure dispensing system. Chapter 3: Process Compatibility outlines available printing modes, available materials and process congruence techniques. Chapter 4: Hardware design details the specifics of the machine design including error budgeting. Chapter 5: Evaluation reports on some critical metrics of process and machine repeatability. Chapter 6: Applications presents various novel prints which were made possible using the hybrid system. Chapter 7: Summary and Future Work recaps this work and discusses potential avenues for further research.

In summary, the principal contribution of this work is the development of a novel hybrid additive manufacturing process, comprising a multi-material direct-write extruder and a drop-on-demand inkjet. This includes newly enabled printing modalities and the non-contact registration between the two processes. Preliminary applications are then demonstrated.

Chapter 2: Background

This section will give a brief overview of the theory behind multi-material inkjet additive manufacturing with a particular emphasis on photopolymers, as well as the governing equations for time-pressure deposition. Both of these technologies can be considered forms of direct-writing (DW), according to the classification presented in [3], however many other works, including this work, treat them separately. A high-level introduction to the custom inkjet set-up used in this work will also be presented as it is necessary to understand the process as a whole.

2.1 Inkjet Theory

A drop-on-demand (DoD) inkjet head consists of an array of nozzles, each with its own individually addressable piezoelectric element. An applied voltage to the piezo causes deformation, which reacts against the fluid above the nozzle and causes the formation of a droplet. In practice, a waveform of particular amplitude and frequency is needed to permit the proper ejection of a droplet and refilling of the fluid channel. This waveform must be optimized for a particular fluid.

In addition to the tuning of the waveform, there are many considerations on the fluid rheology. Specifically, an empirical model for proper jetting known as Z number (which is the reciprocal of the non-dimensional quantity known as the Ohnesorge number) states that the viscosity and surface tension of the fluid must lie in the range of $1< Z < 10$ [21] with Z defined as follows:

$$Z = \frac{\sqrt{\gamma \rho a}}{\eta} \tag{2.1}$$

Where γ is the surface tension, ρ is density, a is the characteristic length (nozzle diameter) and η is the dynamic viscosity. This and other important relations can be found in a review by Brian Derby [22], including a more detailed plot of stable jetting region with respect to Reynolds number, Weber number and Ohnesorge number. It is common place in photopolymer jetting to increase the jetting temperature to decrease the fluid's viscosity into the acceptable range. For the hardware in question, this is typical 5-20cps. Other fluid considerations include the maximum particle size, typically taken at 10% of the orifice diameter (in this case, <3μm), and chemical compatibility between the fluid and the materials in the wetted path. This last restriction typically eliminates printing with strong acids, bases and certain solvents.

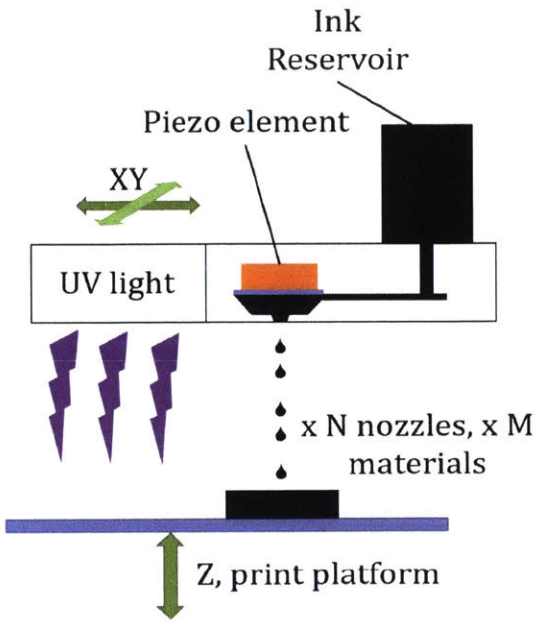

Figure 2.1: Schematic of a single nozzle inkjet system with ultraviolet (UV) curing light. System is mounted to a gantry.

The individually addressable piezoelectric elements allows for the precise timing and positioning of droplets during the print. For use in additive manufacturing, each droplet forms a three-dimensional pixel, referred to as a voxel (for *vo*lume pi*xel*), can potentially be made from a different materials. The number of available materials is governed by the number of available independent channels and/or print heads. Drops can be deposited at rates between 1 and 20 kHz, depending on the model of the print head and the fluid.

2.1.1 Photopolymer Curing

Photopolymers contain a chemically active species known as a photoinitiator which responds to a particular wavelength of light, starting a chemical reaction resulting in the formation of polymer crosslinks. Two different chemistries are often employed: cationic or anionic curing. Cationic curing, otherwise known as free-radical polymerization, works by creating a Lewis acid. As the reaction is not constrained to the volume which saw UV exposure, it has the potential cure shadowed areas. In order for the crosslinking reaction to take place, the photo initiator must be activated by receiving a sufficient amount of energy, often denoted E_c, at the correct wavelength. As the reaction occurs first at the exposed surface, another consideration is the depth of cure, as cured material often blocks sufficient intensity from transmitting through to the uncured polymer. The intensity falls off exponentially with the distance from the free surface. These effects are captured by the Beer-Lambert law [23].

2.2 Choice of Direct-Write Technology

Many forms of room temperature extrusion technologies exist. This section provides a brief overview of the available options and the rationale behind the choice of time-pressure dispensing.

2.2.1 Types of Fluid Dispensers

At room temperature, there exist three primary forms of actuation for dispensing a fluid through a needle-like nozzle: time-pressure, rotary screw, and positive-displacement. This last category may be further subdivided based upon the location of the drive mechanism. Conventionally, a stepper motor is connected to a plunger which pushes directly on ink in a syringe. If this syringe is mounted on the gantry, it will be referred to a conventional type. If the syringe is mounted off-board and the ink passes through narrow tubing before arriving at the nozzle on the gantry, it will be referred to a syringe pump.

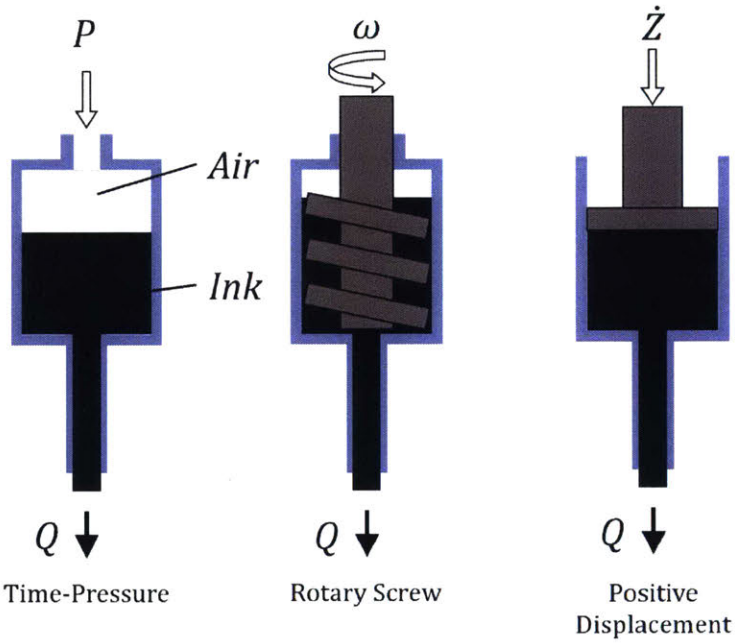

Figure 2.2: Schematic of three different types of dispensing systems (time-pressure, rotary screw and positive displacement) showing their respective inputs (pressure, angular velocity and linear velocity). Adapted from [24]

2.2.2 Selection of Dispensing Technology

Previous work has aimed to axiomatically determine the optimal dispensing technique for a given material, flowrate and accuracy requirements [24]. The functional requirements for this system can be succinctly stated as:

1. Extrude arbitrary fluids (1-500,000cps) through various diameter nozzles (30μm to 2mm)
2. Ensure repeatability of extrudate

3. Be able to scale system to a multiple material variant
4. Take up a minimum of on-gantry space
5. Ease of switching materials

Given the functional requirements encourage versatility as possible, such an approach was not taken here. A comparison table of the considered options can be found below. The rotary screw design was not considered due to the lack of commercially available units and the necessity to clean the screw for material changes.

Table 2.1: Comparison of dispensing technologies

Metric / Technology	**Time-pressure**	**Positive Displacement**	**Syringe Pump**
Inputs	P, ($\dot{m}$)	$\dot{Z}$	$\dot{Z}$
Input dynamics	Flow/compressibility of air	Negligible	Negligible
Ex. Commercial Unit	Nordson Ultimus V with HP3cc adapter	Custom	Harvard Appartus PHD Ultra OEM Syringe Pump 70-3506
Max. Extrusion Force	700psi on 3cc syringe = 350N		334N
Maximum flow rate	Material dependent		216mL/min
Reproducibility	Not quoted		±0.05%
On-gantry space	Minimal	Medium	Negligible
Low viscosity fluids	Yes, vacuum	Yes, retraction	Yes, retraction
Scalability: multi-material	Yes, with pressure output multiplexing	Need N units	Need N units
Material changes	No cleaning	Clean or replace plunger	Clean or replace feed tubing
Dead volume	Nozzle only	Nozzle + tubing	Nozzle + tubing
Unit cost	$5000	Est. $300	$3400

The determining factors here were the material changes and scalability, as this is intended to be a research device. The time-pressure dispensing solution was selected, despite the introduction of an additional dynamic component from the pneumatic system.

The pressure system chosen, the Ultimus V, is a commercially available dispensing system sold by Nordson EFD. The unit is capable of producing an output varying between 100psi and 18 inches of water (vacuum) and toggling the output on or off. The vacuum setting is used when not dispensing to prevent thinner materials from leaking out of a larger diameter nozzle. Further control features include an RS-232 interface for setting the pressure and vacuum settings. This system is not

dissimilar to technology used in bioplotters [25], which have many of the same requirements listed here.

2.3 3D Printing Classification

There exist numerous ways to classify the various forms of additive manufacturing techniques and their subdivisions. Such approaches have looked at the forms of energy used and the area to which it is applied, the types of materials used, or the method for solidification, bonding or sintering. As this system is incredibly flexible, it is challenging to place it uniquely inside of existing classification schemes. Instead, a list of descriptors will be used to describe the capabilities of each of the processes, as well as a list of commonly used process names found in literature.

Table 2.2: List of descriptors for the two printing processes

Inkjet	Direct-Write
Parallel deposition	Without melting
Multijet Printing	Serial deposition
UV-curing photopolymers	Time-pressure dispensing
IR-assisted evaporation	Direct-write assembly or direct-ink writing
	3D-bioplotting
	Low-temperature deposition manufacturing
	Solvent-based extrusion freeforming

2.4 Time-Pressure Dispensing Theory

This section will explain the choice of deposition technology and present steady-state models which capture the fluid flow. One can abstract the time-pressure dispensing process into to four distinct steps:

1. Air is admitted into the syringe, at a particular pressure
2. The applied pressure, along with nozzle geometry and fluid properties, gives a volumetric flow rate
3. The write speed determines the cross-sectional area. A perfectly matched write speed leads to a cross-sectional area equal to the nozzle area.
4. The extrudate geometry is determined via the height of the nozzle off of the substrate, fluid properties, surface interaction, and, possibly, the solidification processes

From a dynamics standpoint, the process can be thought of the combination of the pneumatic and hydraulic processes. As the pneumatic process usually occurs at a timescale of 50-100ms, compared to the response time for the fluid at 10^{-3} to 10^{-6} seconds. This implies the fluid dynamics can be ignored [26]. Furthermore, there are two common modes of operation for time-pressure dispensers: discontinuous or dot dispensing, and continuous or line dispensing. In dot dispensing, it is essential to control the drop volume accurately. This process is highly dynamic and so air and fluid compressibility, as well as overcoming the surface tension at the nozzle are major factors. Additionally, it is known that in this highly dynamic setting, there is decrease in drop volume as the fluid level in the syringe decreases due to the increase in the volume of air which must first be compressed. This work is largely concerned with the latter, and so the dispensing will be modelled as steady-state.

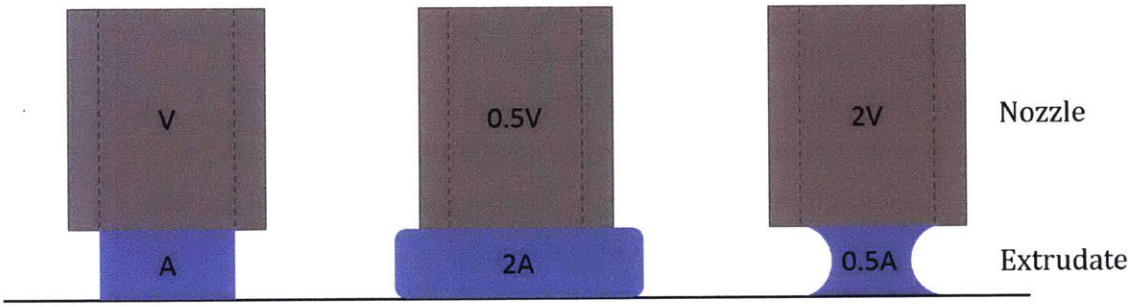

Figure 2.3: Schematic of direct-write process showing the effect of the write speed (V) on extrudate cross-sectional area (A). A perfectly matched write speed will have the same cross-sectional area as the nozzle orifice (A). Write direction is into page.

However, the pneumatic system dynamics do play a role during the start and end of an extruded line. A start-up delay and shut off distance are commonly used in such systems to compensate for dynamics in the pressure system [27]. A simple scheme would have a look ahead, and, using the feed rates, turn the pressure on a specified time before the start of an extruded road and shut it off slightly before or after, depending on the fluid. Strictly speaking, this should be done as a function of the volume remaining in the syringe to account for the compressibility of air. This effect will be shown to be negligible in Chapter 3, and so volume-dependent time-padding is not explored further in this work.

2.4.1 Extrudate Cross-section

It is important to know both the extrudate cross sectional shape and area. A simplistic model based around the conservation of volume can be useful in predicting the cross-sectional area. Previous work has sought to develop models which can predict the geometry which exits the nozzle based on operating parameters. A study looked at the horizontal line widths only for different nozzle

diameters, feed rates and applied pressures and considered non-Newtonian effects with a power law viscosity model [28]. The extruded roads had a very high aspect ratio: 30-60μm wide and only 2-3μm high. Another study combined physical and experimental data to develop a model to predict both the extruded height and width under similar input changes [29]. However, this study used a photocuring polymer chemistry and the cross-section resembled a half-ellipse and includes. Geometries printed with highly shear-thinning fluids can be approximated by a full ellipse. Due to the sheer number of factors involved and the wide library of fluids available, the cross-sectional geometry will be explored experimentally in Chapter 5.

This leads into an extension for printing stability. In general, it is desirable to increase the printing speed for throughput considerations. It has been reported that the minimum area achievable (at the maximum write speed) is stable up to

$$A_{min} = \frac{l^2}{\pi} \tag{2.2}$$

Where l is the distance between the nozzle tip and the surface [30].

2.4.2 Fluid Properties

A wide variety of materials are available for use in the system as there are very few rheological limitations. For any sort of prediction of dispensing behavior, it is essential to understand the properties of the ink in question. Fluids can be broadly divided by their behavior under shear stress into Newtonian, non-Newtonian. Non-Newtonian fluids can either thicken or thin with increasing shear rate; only the latter is considered here. Furthermore, fluids can be categorized by the existence of a yield stress (τ_y) or not. Those will a yield stress are known as Bingham fluids. Fluids which exhibit time-dependent fluid properties, known as thixotropic fluids, are not considered in this work.

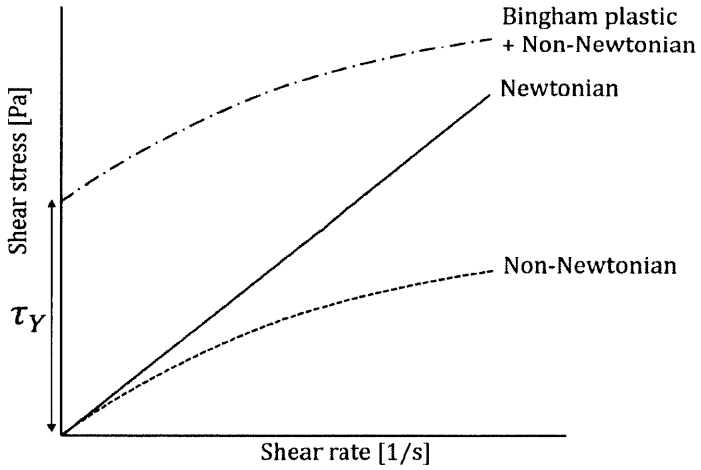

Figure 2.4: Plot of the shear stress versus shear rate relationship for the fluid models of interest

Clearly, some fluids have viscoelastic behavior. A fluid's yield point, if it has one, can be found experimentally by finding the cross-over point between the storage (G', elastic, solid-like effects) and the loss (G", vicious effects) moduli. This can be determined experimentally by performing a frequency sweep with a viscometer and plotting the G' and G" against shear stress. The point at which the two moduli intersect is known as the transition point [31][32].

In general, those fluids which are capable of retaining their shape after extrusion (and spanning small gaps) are those with a high yield stress and large shear-thinning behavior. An ideal material yields, thins such that it can be extruded through a fine nozzle with reasonable force, and then recovers quickly to hold the printed geometry.

Lastly, viscosity is often a function of temperature, and is often experimentally fitted to an Arrhenius model [26]

$$\eta(T) = \mu_0 e^{T_k/T} \tag{2.3}$$

where μ_0 is the base viscosity and T_k is an experimentally fit temperature correction factor. In this work, this is only used to correct the model to the ambient conditions during as deliberately heating or cooling the fluid is not investigated.

2.4.3 Newtonian Flow Rate Model

Under the steady-state assumption, the question of volumetric flow rate will be addressed theoretically and verified experimentally.

As a first order approximation, the gauge pressure required to extrude a Newtonian fluid out of a nozzle is given by the Hagen-Poiseuille equation [33]

$$P = \frac{128\eta LQ}{\pi d^4} \qquad (2.4)$$

where η is the kinematic viscosity, L is the characteristic length, Q is the average volumetric flowrate and d is the diameter of the pipe. This relationship assumes laminar, fully-developed flow, with a no slip condition, no effect of gravity head (horizontal pipe) and neglects any frictional losses. As the Reynolds number is so low, it is appropriate to drop any frictional effects from the model.

A simple MATLAB script was developed which allowed for the visualization of permissible fluid viscosities based upon the available pressures from the chosen commercial system (700psi, with a high pressure adapter), gantry speed limitations (approximately 200mm/s) and a continuous sampling of commercially available nozzle diameters and a fixed nozzle length (15mm). The following limiting surface for dynamic viscosity was obtained.

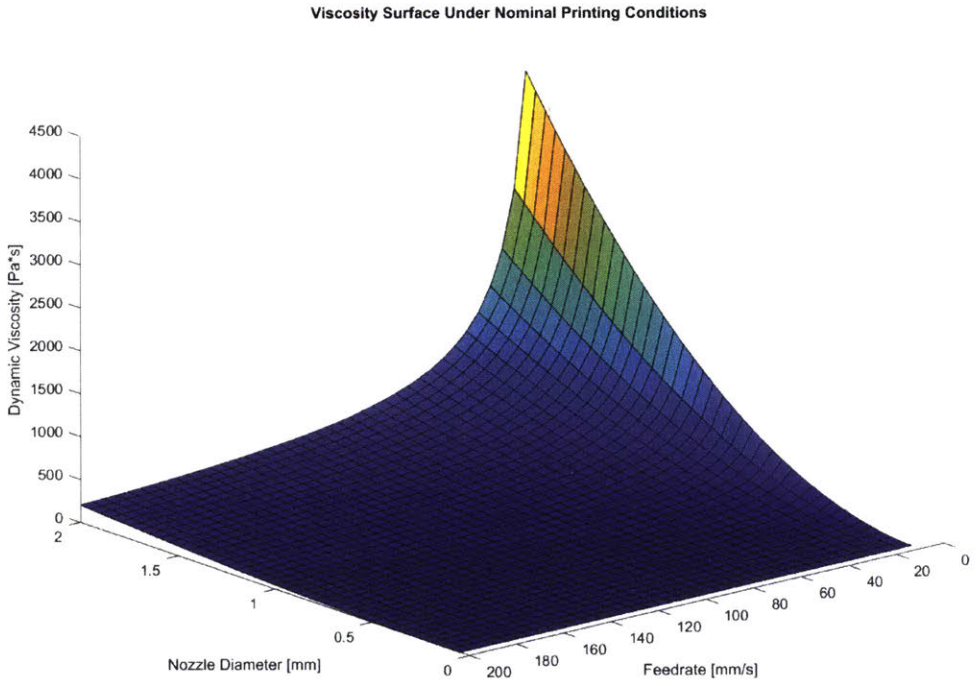

Figure 2.5: Viscosity surface under nominal printing conditions

All points were verified to have a Reynolds number much lower than 2300, validating the laminar assumption. It is evident that the maximum viscosity can be several orders of magnitude above the inkjet process. It is also apparent that the most sensitive parameter is the nozzle diameter, as this term is the fourth power in the pressure equation. It should be noted that high-loading

colloidal inks are known to undergo plug flow, and many of the inks in question are shear-thinning with a yield stress and so this model does not properly capture all fluids of interest [34].

2.4.4 Power Law Flow Rate Model

In the printing window, most fluids of interest exhibit shear-thinning (non-Newtonian) behavior which can be captured with a power law fluid model

$$\eta = K(\dot{\gamma})^{n-1} \tag{2.5}$$

where K is the fluid consistency index (Pa*s^n), $\dot{\gamma}$ is the effective shear rate (1/s) and n is the power law exponent. It should be noted that the power law is known to break down at the extremes of the variables [35], however the theoretically calculated shear rates lie well within the experimentally obtained data, where the power law model is a good fit.

The effective shear rate inside of a tube is determined by differentiating the axisymmetric fluid velocity profile and is given by [36]

$$\dot{\gamma} = \frac{16Q}{\pi d^3}\left(\frac{3n+1}{2n+1}\right) \tag{2.6}$$

Combining these definitions with the Hagen-Poiseuille equation yields the following as a prediction of extrusion pressure, as presented in [26]

$$Q = \frac{n\pi d^3}{8(3n+1)}\left(\frac{DP}{4LK}\right)^{1/n} \tag{2.7}$$

The equation can easily be arranged to solve for flow rate instead of pressure. It should be noted that when n=1, this equation is exactly the Hagues-Poiseuille equation. This model was implemented in a MATLAB script, allowing the user to calculate either the required printing pressure, or the predicted volumetric flow rate, based upon the fluid properties, traverse speed and nozzle geometry.

2.4.5 Herschel-Bulkley Flow Rate Model

As an extension, a model for the volumetric flow rate which incorporates a fluid's yield stress (Herschel-Bulkley fluid) is presented in [37], and aligns closely with Equation 2.8 for the fluids and shear rates of interest. A Herschel-Bulkley fluid model has three paramters: yield stress (τ_Y), consistency index (K) and a power law exponent (n)

$$\tau = \tau_y + K(\dot{\gamma})^n \tag{2.8}$$

It will be shown that the power-law fit presented above is sufficient to model this process.

2.5 Summary

In conclusion, the inkjet and direct-write processes are governed by much different physics and have different limitations in terms of fluid properties. Many different parameters feed into the control of the dispensing process: applied pressure, nozzle diameter, fluid viscosity (including shear thinning effects, temperature), write speed, offset between the substrate and the nozzle tip, and auxiliary effects.

(this page intentionally left blank)

Chapter 3: Process Compatibility

This chapter discusses how the two processes can be integrated at a high level, including their digital representation and geometric congruence.

3.1 Printing Modes

There exist several possible ways to combine the two processes. They are described below and outlined graphically with the accompanying figure. Horizontal striations indicate show some integer number of inketted layers, where appropriate.

- **Conventional print:** the extruded roads exist as some fraction of a printed layer. Consideration must be given to the physical dimensions of the road and for the extruded road's height to be integer multiple of the inkjet layer height. The deposition order is not specified.
- **Embedded printing**: the extruded road is placed within an uncured material. Out of plane features are possible. The densities of the two fluids must be very closely matched and the uncured material must have the appropriate properties to flow in behind the nozzle.
    - A subset of this is the filling of cavities or wells previously created with a structural material.
- **Contour printing:** the nozzle follows the contours of pre-printed geometry. The offset between the nozzle and the substrate should be computed with consideration for the effective slope of the underlying surface.
- **Reactive chemistries:** chemical species are inkjetted onto extruded geometry which change the mechanical properties in some fashion
- **Release layers:** depositing a thin, inert layer that can be used as a release agent for other geometries. While functionally similar, these materials differ from conventional support materials due to their thickness.

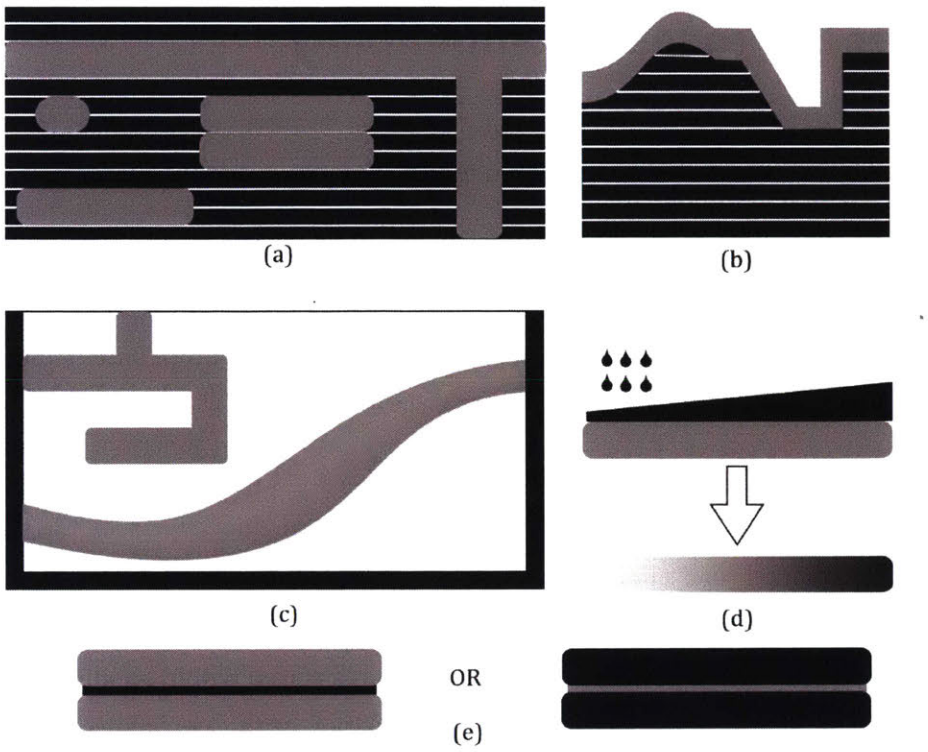

Figure 3.1: Various printing modes: (a) conventional (b) embedded (c) contour (d) reactive (e) release. Black denotes inkjet and grey denotes direct-writes geometry.

Additionally, the time-pressure system can double as a crude pick and place machine. Experimentation using the vacuum setting of the Nordson EFD system (18 inH_20) was used to pick up IC's weighing approximately 0.1g. Other researchers arrived at the same technique, as demonstrated in [38].

3.2 Digital File Representation

While not the focus of this work, it is important to understand the distinction between the digital representations for the two separate process combined in this machine. Traditionally, most machines with a single tooltip in a Cartesian arrangement (or, with a less standard architecture that can be mapped to independent axis motions) are controlled using G-code. The pressure-based extruder falls into this category. Fundamentally, G-code is human-readable representation of machine motions; way-points and speeds are set and the machine's controller must do its best to reach and interpolate between these positions at the specified feed rate. Higher level functions such as spindle and coolant control are usually integrated as well as M-codes. While some controllers offer the ability to follow contours such as arc segments and B-splines natively, the naive implementation discretizes all toolpaths into a large number of waypoints and linearly interpolates between them.

For this reason, G-code should be seen as a *vector* representation (speed & direction) of the tool point's motion. In the case of a three axis Cartesian gantry, all axes have to work together to achieve the requested motions.

Typical workflows for generating G-code include Computer Aided Manufacturing (CAM) software packages for subtractive operations or slicer software for additive processes. Most slicer software have been written especially Fused Filament Fabrication, however it is generally trivial to modify the outputs to suit. One caveat is that slicer software generally aim to infill the entirety of a volume, or create a certain number of roads around the perimeter and fill the remainder with a predetermined pattern and density. Additionally, they generally work layer-wise and there is no notion of aforementioned embedded or contour printing modalities.

Conversely, the inkjet process is a serial process which requires the simultaneous control of a large number of individual nozzles. During a printing pass, the gantry only moves along the primary axis (X). For full coverage, there is then a step-over in the secondary axis (Y) and another printing pass on the primary axis. The tertiary axis (Z) only moves between individual layers to maintain the correct distance between the printed geometry and the face of the print head (or to maintain the correct layer height, in the case when a levelling roller is installed). While positioning must be repeatable between subsequent printing passes, another important factor is the primary axis speed, which should ideally be constant. In an open-loop control scheme, the print head is ramped up to (assumed) the desired speed. Shortly thereafter, the actual deposition occurs in a time-dependent manner. It is important to note that only one axis need be controlled at a time in this setup. Additionally, with some abstraction, the file format should be thought of as a *raster* image file (i.e. a series of pixels) which must be filled with the correct material. As the geometry created is 3D, the actual representation is done with voxels (*vo*lume pi*xels*).

In order to make the spatial material assignments for the inkjet geometry in the simple case where there are few (or very discrete transitions) between different materials, multiple STL files, each representing the geometry occupied by one material, are loaded into a custom script. The script divides the volume into the appropriately spaced 3D grid of voxels with the material assignments.

On the process side, only one of the deposition techniques occurs at time. In other words, the printer may transition from *raster mode* to and from *vector mode*. Choosing the points in the process to transition is non-trivial and relies heavily on the designer's intent.

For this thesis, the generation of files combining both the vector and raster representations was performed manually. A system which allows a designer to work natively with both representations and all the aforementioned printing modes, which also prepares the file for printing with the necessary transitions between modes, is an active area of research.

Furthermore, it should have some automation for infill pattern generation and scaffold geometries. Additionally, it should operate on a wide range of length scales (from μm to m) and natively support the material assignments. It should be clear that the envisioned software package must have many features for which traditional Constructive Solid Geometry (CGS) and Boundary Representation (B-rep) packages are not well-suited.

3.2.1 Print File Preparation

In the majority of cases, the current workflow involves the use of commercial CAD/CAM software (SolidWorks with HSMWorks plug-in) and manual post-processing to generate the vector files for printing. The generated G-code file must adhere to the chosen subset of G and M commands listed below.

Table 3.1: Selected G-code implementation

Command	Description	Example	Comments
G01 X# Y# Z# A# B#	Move command, mm	G01 X3.5 Y3.5 F8.0 P15.0	In practice, only 3 of these are used in any one program
F#	Feed rate, mm/s		Modal and optional
P#	Pressure on, at specified psi		Modal and optional. P0 shuts off trigger.
V#	Vacuum on, at specified inches of H_20		Modal and optional
G92 X# Y# Z# A# B#	Set position	G92 X0.0 Y0.0 Z0.0 Sets current position as origin	In practice, only 3 of these are used in any one program. No motion occurs.
G04 S# P#	Dwell	G04 S0.5 P1	S in seconds
T	Tool selection	T01	
M06	Execute tool change		
G20/21	mm/in mode		
G90/91	Absolute/Relative mode		
M205 X# Z#	Junction Deviation		A simplified jerk parameter, as used in Smoothie/Grbl [39]

As discussed, a custom voxelizer is used to generate the raster file.

3.3 Deposition Rates and Resolutions

While there is no stringent requirement on the throughput for this process, a first order analysis was performed comparing the two processes. As the inkjet process is parallelized and the direct write process is serial, they are compared solely on the basis of volumetric flow rate.

The maximum volumetric flow rate of the time-pressure dispenser is heavily dependent on the viscosity of the fluid. In many cases, this may be limited by the speed of the gantry. From experience, reasonable flow rates can approach 25μL/s or 1.5mL/min. It should be noted that the 10mL syringe (the largest intended for this system) will be depleted in about seven minutes of continuous usage at this rate. Single droplets from the inkjet printheads in question are approximately 25pL. Assuming all of the 540 nozzles are firing at 3kHz with a 30% duty cycle, this leads to a maximum rate of approximately 0.8mL/min.

Another area of concern is the spatial resolution of the two processes. Inkjet drops can typically be placed with an accuracy of 10μm and micro deposition systems are able to create micron scale features. Here, the minimum feature size is governed by the repeatability of the gantry – about 5μm. Typical extrudate widths for this work are approximately 500μm, which can be considered macroscale with relation to a single inkjet voxel.

3.4 Available Materials

The repository of materials which can be processed by inkjet and dispensing processes is constantly growing. A high level categorization is presented in the chart below, with a few representative examples for each category. It should be noted that some categories are not mutually exclusive. Ultimately, the determination of which deposition system to use is largely a function of the ink properties, and to a lesser extent the desired geometry.

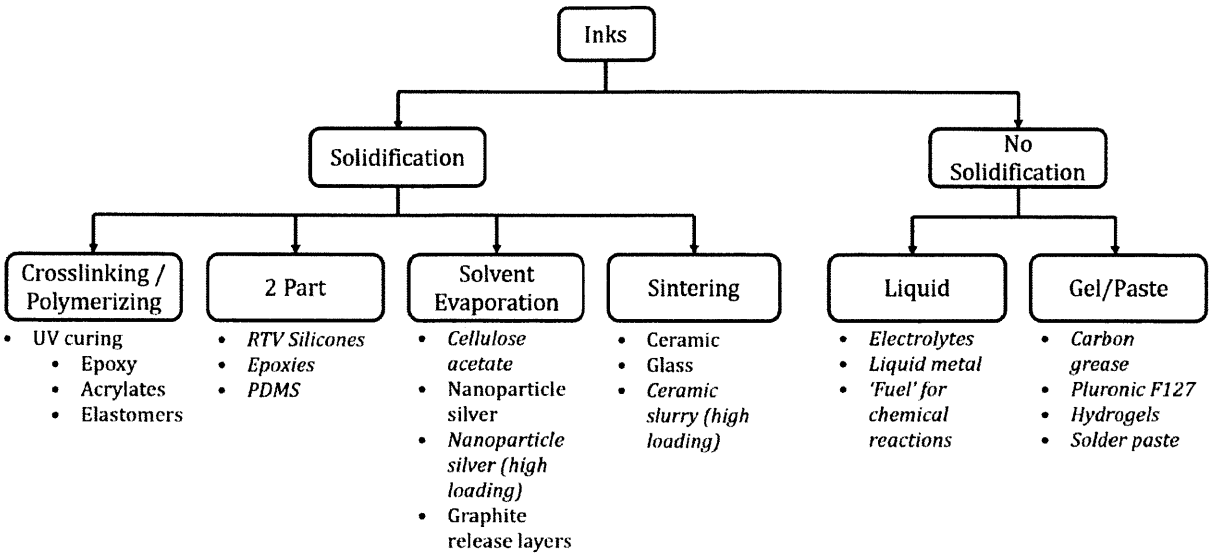

Figure 3.2: Classification of available inks. Italicized examples are best suited to the time-pressure dispensing process.

3.5 Conventional Printing Considerations

As the inkjet process accuracy is fairly sensitive to the offset between the substrate and the faceplate, the printing process needs to be made planar (in conventional printing mode). The process for changing between the two modes of deposition is straightforward, but one must be conscious of where in the file the transitions are made. A discussion of how to schedule the inkjet and direct-write processes follows. Additionally, these two processes must have a high degree of geometric congruence for part geometric fidelity.

3.5.1 Sensitivity Analysis

In an open-loop, conventional printing mode, any systematic or random errors in the extruded geometry will lead to a propagation of errors. Going forward, the inkjetted geometry will be taken as the ground truth, despite the fact minor variations in drop volume do occur.

After performing a one-factor-at-a-time sensitivity analysis, it was determined that variation of the process is potentially quite large, with even minimal changes in the parameters. For representative sample numbers ($K=350 Pa*s^n$, $n=0.35$ $d=0.5mm$, $L=17.5mm$, $P=22psi$), the plot below shows the impact of reasonably assumed variations in the process dimensions. Intuitively, the process is most sensitive to both the diameter of the nozzle and the experimentally fitted power law constant, n. The 3.5% (each side) spread on the diameter corresponds to published values of nozzle inside diameters from some manufacturers.

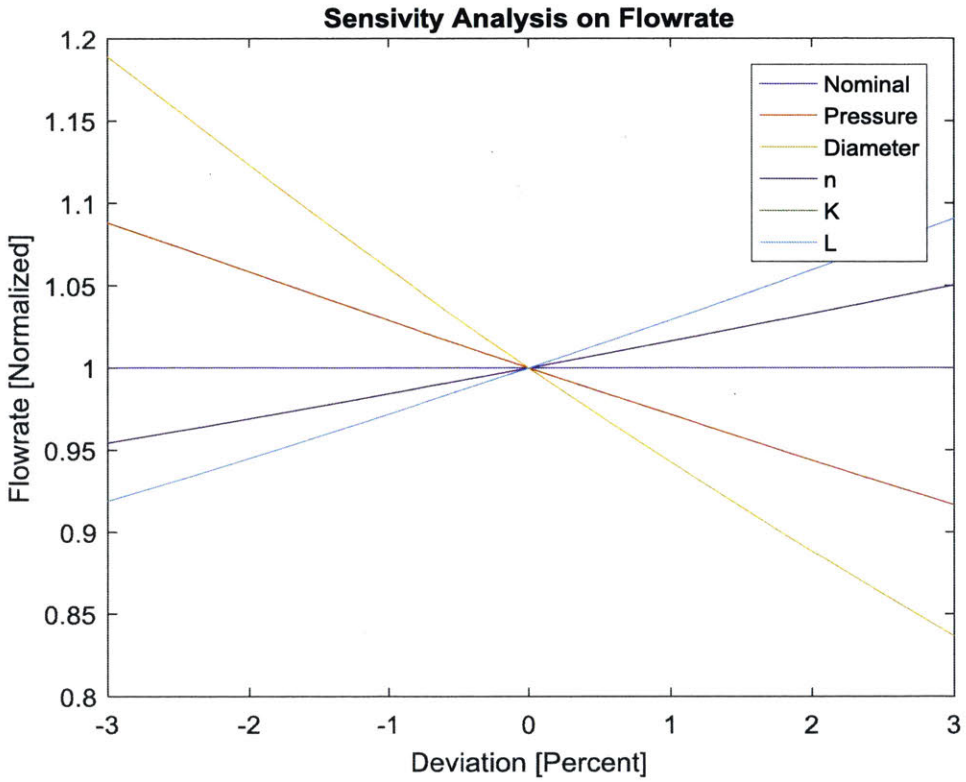

Figure 3.3: One factor at a time sensitivity analysis of flowrate on input parameters: pressure, nozzle diameter, fluid power-law consistency index (n), consistency index (K) and nozzle length (L). Results are normalized.

While diameter and pressure appear approximately linear in this regime, they are in fact non-linear. For a three percent variation in nozzle diameter, the flow rate can be almost 20% off. This analysis should be repeated for the actual nominal values in use as importance of the parameters scales with their relative magnitudes. Previous work presents some findings on ranges with minimal variance, concluding that operating at higher pressures is favorable [26].

3.5.2 Matched Cross-section Technique

In principle, the limiting factor is that the inkjet cannot deposit material underneath a feature which has already been deposited. This means that the print should be split at the Z-level where the extrudate geometry is the widest. Any errors in the direct-write process will directly propagate to the subsequently inkjetted geometry.

3.5.3 Well-printing Technique

A technique was developed to simplify the printing routine and average out any variance in the direct-write process. The technique involves dispensing the fluid into an oversized cavity or well, and then filling the well with uncured material.

Normally, the inkjetted geometry is cured after each pass. In this technique, a larger volume of inkjet polymer is deposited into a pre-printed container or well, and allowed to settle. It was observed that at above some critical thickness, the polymer is self-levelling (except for meniscus effects). By performing this technique after an extruded road has been printed, one need only match the volume of the extrudate. Any local imperfections in the extrudate, especially at the start or end of a trace, is averaged out over the entire fill volume. This approach functions so long as the extrudate is not miscible with the infilling material, and the infill layer is sufficiently small in thickness and volume to prevent a buildup of residual stress as it cures. An alternative method would be to dispense a two-part material, such as an epoxy. These materials can be formulated to exhibit minimal shrinkage.

There is a limit as to how much photopolymer can be cured at one time, both in overall volume and in thickness. The first is governed by the polymerization reaction kinetics – the process is exothermic. The second is governed by the Beer-Lambert law for intensity as a function of distance [23].

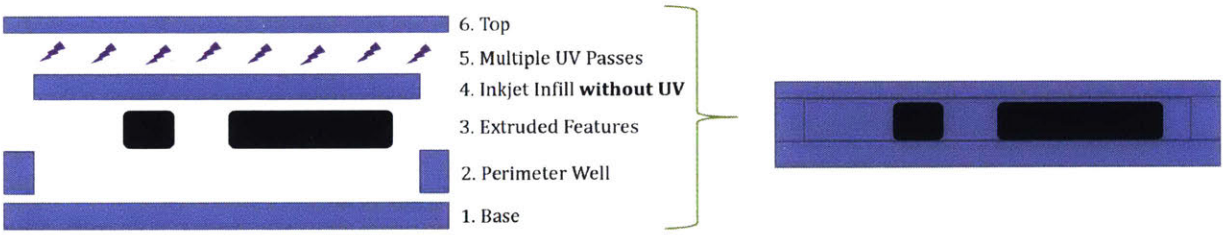

Figure 3.4: 2D schematic of well printing technique, showing various printing steps (left) and final geometry (right). Blue is material deposited by inkjet; black is material deposited via direct-write.

3.5.4 Z Via Technique

To make a connection between layers of extruded geometry, a four step approach is recommended. First, the base layer is created via inkjet deposition. Then, the lower extrudate is made. This is followed by an additional inkjet layer, leaving a hole in place at the desired point to interconnect. The uppermost extrudate deposition is then programmed with a plunge into the hole to create the connection.

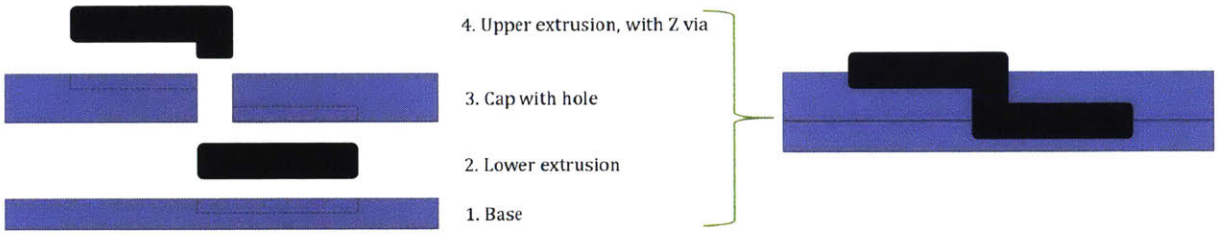

Figure 3.5: 2D schematic of Z via printing technique, showing various printing steps (left) and final geometry (right). Blue is material deposited by inkjet; black is material deposited via direct-write.

3.6 Summary

In summary, the designer must be conscious of the many different printing modes available, as well as any material limitations, especially in terms of their interactions. Scheduling of the two processes remains a designer-involved task, especially due to the multitude of different material solidification mechanisms and cross-section compensation techniques.

(this page intentionally left blank)

Chapter 4: Hardware Design

The design of the hardware was performed in a prototype and a more refined version. The prototype system will be discussed briefly; most of this section will focus on the machine design for the second iteration which had many improvements.

4.1 Prototype system

The prototype system was designed as a retrofit for the MultiFab platform. Initial work was performed with an FDM head in order to work on the necessary firmware and software changes to support vector movement and initial dimensional fidelity verification.

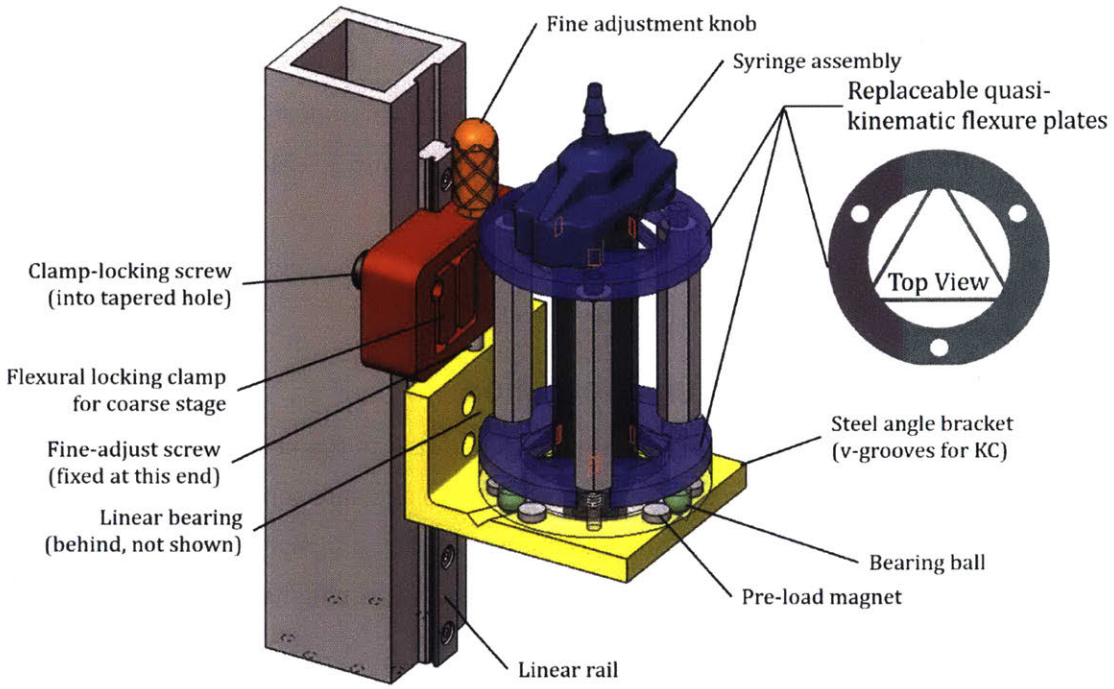

Figure 4.1: Labelled CAD model of porotype setup. Contact areas with the syringe-holding flexures are highlighted.

For versatility, it was desirable to accommodate several of the available syringe sizes; specifically, 3, 5 and 10mL, as well as the 3cc high pressure (HP3cc) adapter. The diameters ranged from 0.45 to 0.75 inches, with the 3cc HP being significantly taller than the others. For repeatable mounting of these syringes to a common center, both a quasi-kinematic and a kinematic coupling were used. The syringes are held in a cage-like structure, which acts at 6 line-contacts via two plates, each with three blade flexures. This cage is then mounted via a standard three ball/groove kinematic magnetically-preloaded kinematic coupling to a precision linear bearing. The Z axis is manually

adjustable, and comprises a coarse and fine stage. An acetal clamp, based upon an in-plane flexure design which delivers equal clamping pressure [40] so as not to damage the rail, locks the Z position of the coarse stage. The linear bearing is suspended from this clamp by a fine-pitch screw, which allows for fine adjustment of the Z height.

Preliminary testing using this setup validated the process and highlighted a few areas for improvement:

- The process is extremely sensitive to the offset between the extruder tip and platform. While touching off the nozzle to the substrate and moving the Z axis away the desired amount is acceptable for some applications, this is unacceptable for a 30μm glass nozzle.
- While the kinematic arrangement is sufficiently repeatable, it cannot account for concentricity issues between different nozzles.
- The cross-section of the extruded road is of critical importance to the process. Being able to predict the shape, or at least the area, *a priori* is a requirement for successfully merging the two processes.
- Fluid rheology is highly sensitive to temperature. Space permitted, the syringe should be mounted further from UV LED heat sink.

4.2 Brainstorming of Second Generation

The second generation system was designed to be fitted to the newest revision of the inkjet printer, on an existing X' axis. This system was designed to alleviate some of the challenges of the prototype system, as well as offer an automated method of changing materials mid-print to expand the processes capabilities. In summary, the main functional requirements included:

- Support the 3, 5 and 10mL syringe as well as the 3cc high pressure adapter
- Allow for rapid, automated switching between four different materials
- Fit into the existing space envelope and cover the entire print platform
- Automated method of determining nozzle tip location in X, Y and Z
- Tooltip position repeatable to 30μm or better

The limited space on the axis and requirements for mounting a scanner on the same carriage (which must also have full coverage of the build platform) greatly influenced the choice of architecture. It was determined to be infeasible to mount the syringes in any static array pattern as the change in tooltip XY position limited the print substrate coverage of the direct-write processes

or the scanner. Variations on a revolver-like (carousel) solution were preferred as the active syringe always exists at the same location and this packaging arrangement was sufficiently compact for mounting the scanner. Conventional tool-changing solution were considered as well, however due to complications with wiring (each syringe requires a pneumatic tubing connection), this was abandoned.

Many options were considered for how to store and actuate the four syringes. They can largely be classified into two schemes regarding the Z actuation: a continuous or a discrete solution. Within the discrete space, there is the potential to have the user set the nozzle tip position with a fine adjustment screw to a known reference height, or to have the sensor be able to move in Z. One of the more elegant solutions was the use of an off-axis rotating turret. This was not pursued as the delta between the lowered, engaged syringe tip and the next lowest syringe tip was only about 0.5mm, making contour printing into deep valleys impossible. Another solution was to have an in-plane rotating turret which passively lowered the active syringe by way of a cam (with a large dwell) and follower. This was not selected for similar reasoning: the maximum achievable delta within the packaging constraints was only 2mm.

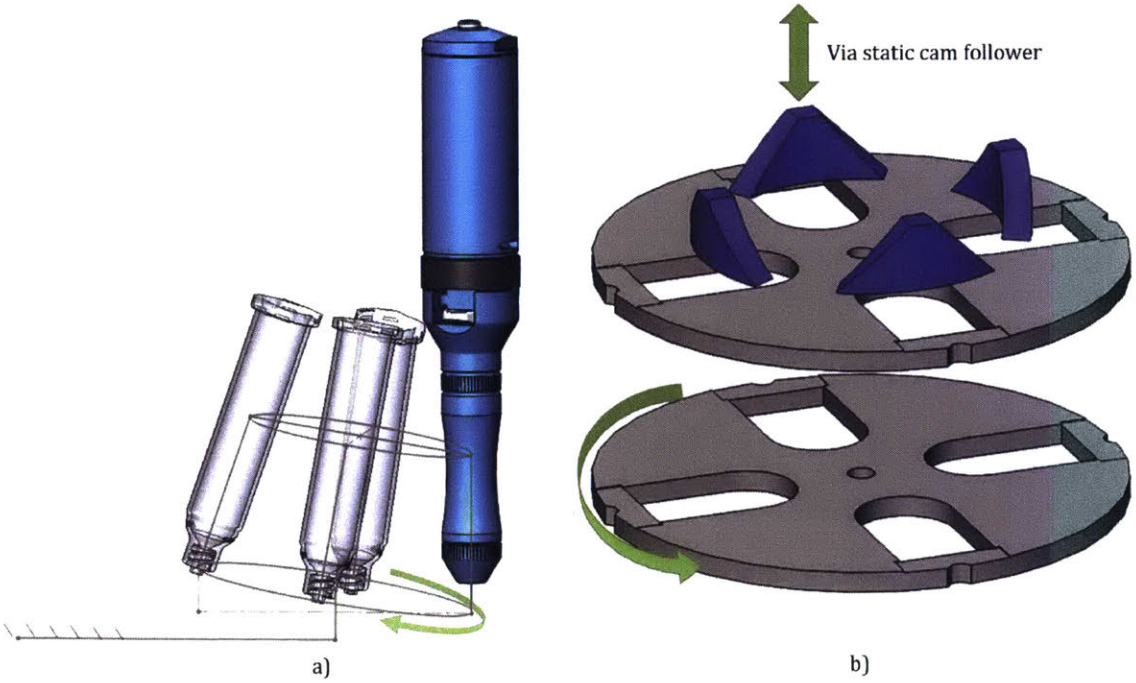

Figure 4.2: Concepts for packaging four syringes on a rotary carousal. a) Achieves lowers the syringe via an off-axis design. b) Utilizes a cam follower and a cam with a dwell period to lower the syringe.

While in some ways redundant, as the printer now has two independent Z axes, a continuous active Z axis was chosen for the syringe. The primary advantages of this architecture is the ability to

drop only the working syringe by approximately three inches for contour printing and the alleviation of any manual calibration routine for the operator while installing the syringes. Furthermore, this axis could be easy instrumented for increased repeatability.

4.3 Overview of Design

For this chapter, the following nomenclature will be used for the axes: X and Y represent the axes used in the inkjet printing process. Z is the axes associated with the print platform. The direct-write process shares the Y axes, while it runs on a different X axes, denoted X'. It can also lower the active syringe by using the Z' axis. The design was carried out to minimize the number of precision machined components.

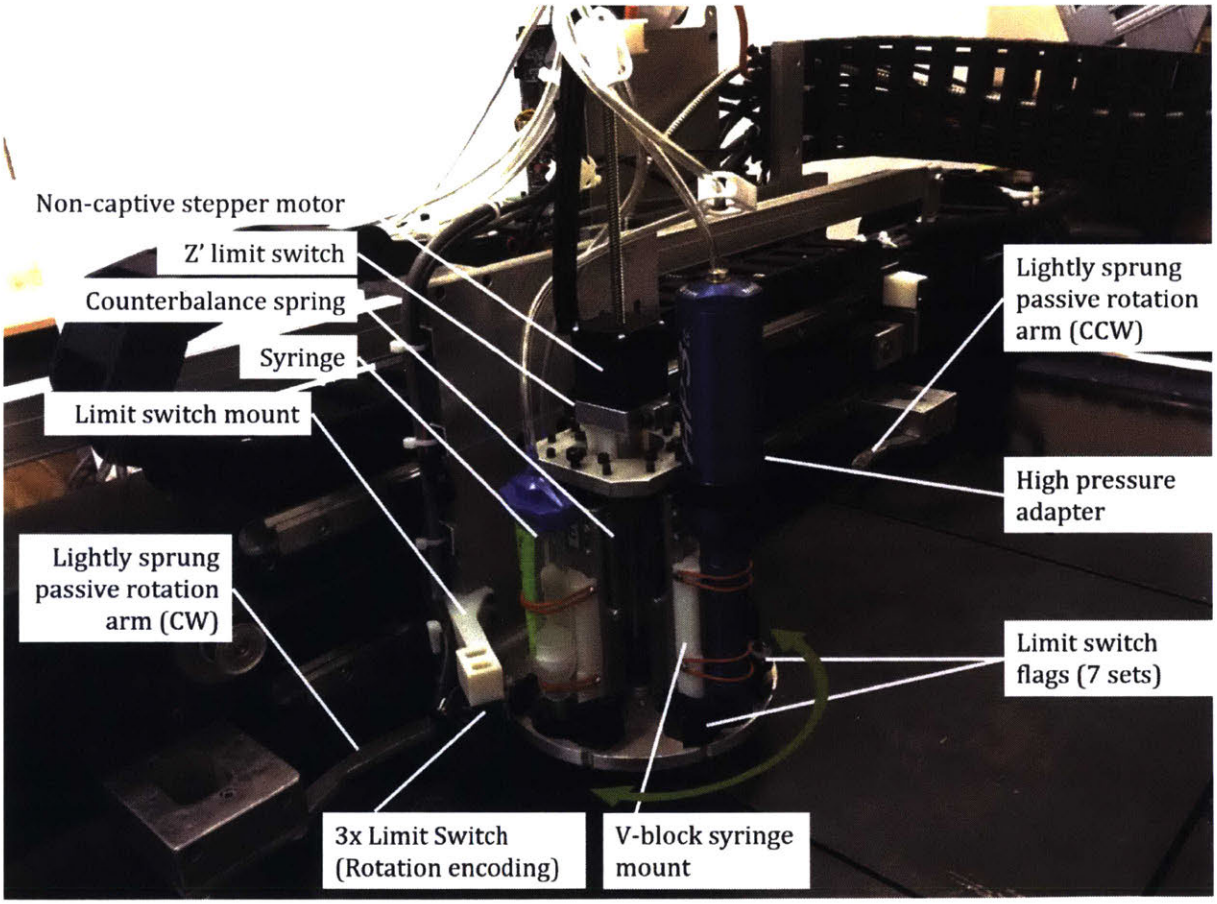

Figure 4.3: Photo of labelled direct-write carousel assmebly mounted to gantry.

Due to the space constraints, a passive rotation mechanism was employed. Two lightly sprung arms exist at the extremes of the X' axis and engage on pins around the circumference of the turret. Moving the X' towards its minimum leads to a 45 degree rotation clockwise (looking top-down), while

an equal counterclockwise rotation occurs at the other X' extreme. A spring detent is responsible for the repeatability of the turret rotations.

Originally, the detent was a single cantilever arm, which could not react against moments. Consequently, there was some directionality involved with its repeatability. The second revision of the arm featured two cantilevers spaced apart, which allows for the structure to act against moments imparted from the v-groove. The contact point was made from wear-resistant acetal such that it wears preferentially to the aluminum surface. While better repeatability can likely be obtained with a precision ground steel or ceramic dowel, the decision to use a polymer is justified from a serviceability standpoint. An external compression spring is used and was sized in order to give an appropriate seating force, while being loose enough to allow for the passive rotation without causing the X' axis motor to loose steps.

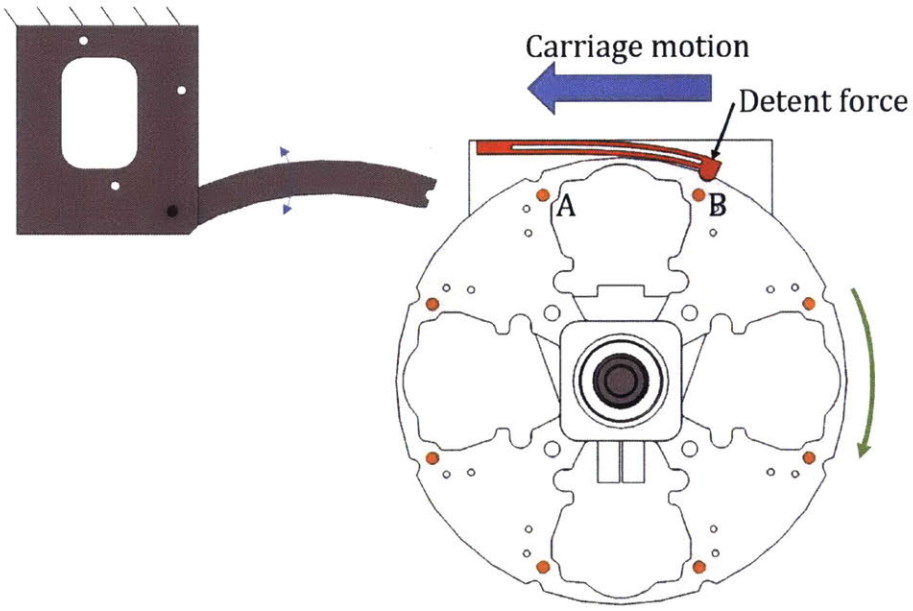

Figure 4.4: Top-down view of carousel base plate and detent (red). The passive rotation arm engages with the protruding dowel pin (orange) and rotates the plate 45° clockwise as the carriage plate is driven into it. Pin A terminates at position B. A mirrored version of the assembly exists at the other extreme of the X' axis and rotates the plate counterclockwise.

A non-captive stepper motor was used as the Z' axis as it could easily be disengaged from the active syringe. The syringes mount to a v-block, which is connected to a sheet metal bracket connected to the precision linear rail (2μm running parallelism). The bearing assembly is counterbalanced by two extension springs. The spring rate was sized to overcome the force of gravity and friction when the heaviest possible syringe is loaded, full of a dense fluid, yet low enough that the non-captive stepper motor can fully extend them.

Figure 4.5: Cross section of carousel assembly in raised state (left) and lowered state (right). The position of the non-captive stepper motor shaft and slider block with drive pin (pink) can be seen inside of the drive tube (transparent blue). Also shown are the bearing block (red), linear rail (green) and the counterbalance springs. Only one syringe rail assembly shown for clarity.

4.4 Error Budgeting

A detailed error budget employing Homogenous Transformation Matrices (HTMs) was used to estimate the errors caused by various mechanical elements in the serial chain from the print substrate to the extruder tip. This process was greatly facilitated by the Excel spreadsheet developed by Professor Alexander Slocum [41]. The spreadsheet was slightly modified to add in a rotary axis for the carousel. This tally was updated often during the design process.

A schematic of the various mechanical elements and their attachment points is depicted in the figure below. Although in theory there are no cutting forces on the tooltip, one can still find the displacements caused by things such as self-weight and running parallelism which propagate and are magnified as angular errors by each subsequent lever arm. For simplicity, the reference ground of this system was taken to be main crossbeam to which the X' axis is mounted. The force imparted by

the detent was included in the model, although its effect was found to be negligible. Additionally, all bolted joints were taken to be infinitely rigid. This assumption is valid due to the lack of significant forces on the gantry structure. All bearings were modelled with their appropriate stiffness from the manufacturer's catalog, if available, or from first principles and an assumed 0.1% deflection on the ball bearings. Furthermore, the two counterbalance springs were assumed to be at the worst case of their published tolerance (±10%), which imparts a moment on the bearing block.

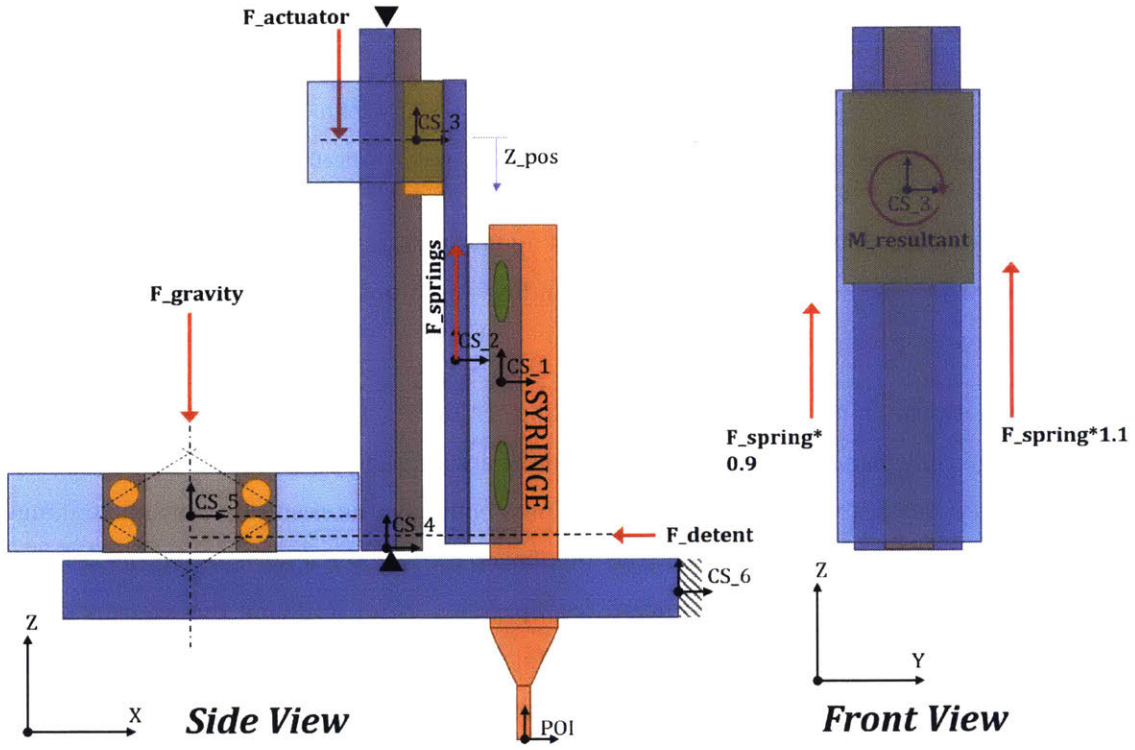

Figure 4.6: Schematic depiction of coordinate systems (CS) used in error budgeting for the tooltip (POI) error. Boundary conditions of the various members and applied loads are shown. Transparency and some items hidden for clarity.

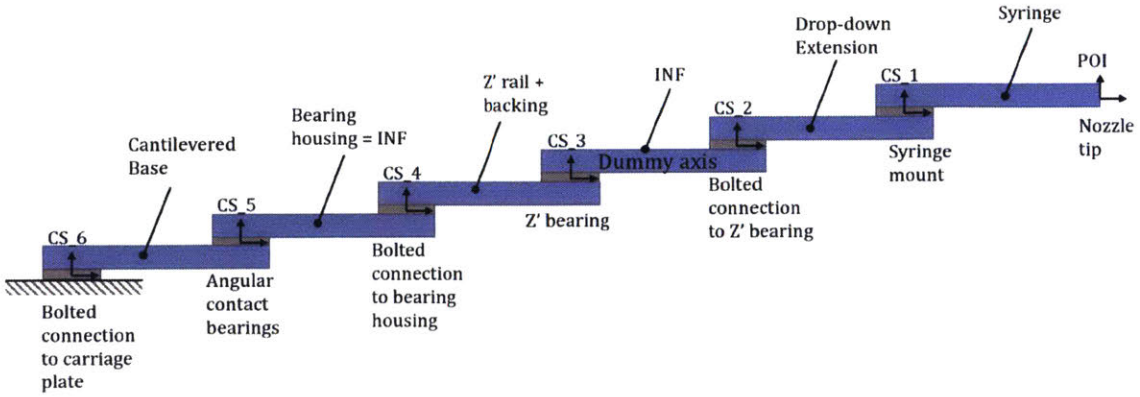

Figure 4.7: Serial depiction of structural loop shown in Figure 4.6 above. Coordinate systems (CS), connections and structural elements are labelled. An independent 6x6 stiffness matrix is applied at each connection and for each element.

In the worksheet, one is able to move both the Z' and X' axis to see the effect of tool position on the tooltip error. The following beam-bending equations drove the position-dependent error gains:

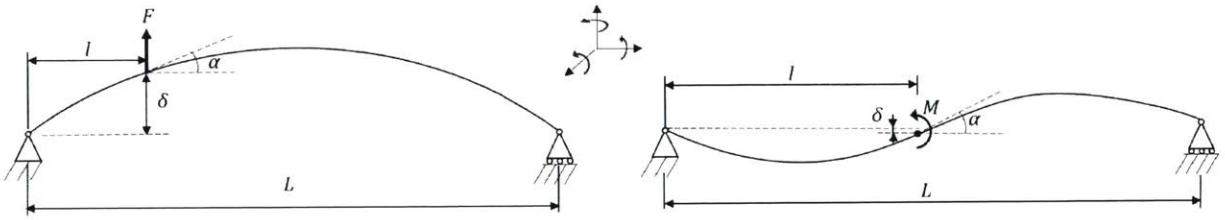

$$\delta = \frac{Fl^2}{3EIL}(L^2 - 2Ll + l^2) \qquad \delta = \frac{Ml}{3EIL}(L^2 - 3Ll + 2l^2)$$
$$\alpha = \frac{Fl}{EIL}(L^2 - 3Ll + 2l^2) \qquad \alpha = \frac{M}{3EIL}(2L^2 - 3Ll + 3l^2)$$

Figure 4.8: Beam bending linear and angular deflection equations used in error budgeting. As these are a function of the linear position along the beam, this allows for modeling as a function of the axis servo position.

It should be noted that some of the structures do not quite satisfy the length to height ratio of 10:1 often quoted for the Euler-Bernoulli beam bending equations to hold. In turn, the predicted deflections and angles presented are conservative.

These equations, along with familiar equations for torsional and axial displacements were entered into a 6x6 compliance matrix for each axis in the error budget. Due to the complicated shape of the cantilevered beam, it was studied in FEA. Conservatively, the resulting normalized angular error was entered to line up with the predicted angular error. Had the displacement been matched, the error budget would have under predicted tooltip error. After applying the appropriate self-weights and fictitious side forces on the tooltip, a total random error of approximately 56μm in the XY plane can be expected, taking the average of the sum and the root mean squared values. The full results are summarized in the table below (at the worst possible position, i.e. the Z' axis fully extended).

All Axes	For the Entire Machine				
	Number of axes	All axes' Geometric Errors			F=kX displacement
	7	Random			
		Sum	RSS	Avg(SUM, RSS)	Sum
	deltaX	0.042284	0.028780	0.035532	0.010645
	deltaY	0.051607	0.036891	0.044249	-0.004416
	deltaZ	0.037629	0.026319	0.031974	0.001675
	Vector displacement	0.076597	0.053683	0.065137	0.011646

Figure 4.9: Output from error budget spreadsheet showing load-induced (F=kX) and random errors at the tooltip

As discussed, the inkjet drop placement process is at best ±5μm, and a single droplet is approximately 35μm in diameter. The predicted tool tip error is approximately two inkjet voxels,

which is acceptable. It is important to note that because of the integration of the optical micrometers, systematic errors are not of concern; only random errors will not be captured and compensated.

4.5 Control

In order to interface with the existing control hardware, the air pressure deposition assembly is controlled by the printer's main electronics board. While miniature magnetic absolute rotary encoders exist, packaging was problematic. The solution was to discretize the rotation states and use three limit switches to determine the current rotational state of the carousel. The limit switches are triggered by mechanical flags on the circumference of the carousel. The truth table which maps the limit switch states, a binary representation, to the rotational states is provided below. Note that the eighth position, all sensors open, is indistinguishable from the state between discrete steps, and is not used (beyond error-checking).

Table 4.1: Truth table for the three limit switches which encode the carousel rotary position. X denotes depressed by a mechanical flag.

Position	1 (A)	2	3 (B)	4	5 (C)	6	7 (D)
Top	X		X	X		X	
Middle		X	X		X	X	
Bottom			X	X	X		X

As the Ultimus V dispenser has a single output, its output is multiplexing using four normally closed, vacuum-rated valves (Clippard DV-2M-12) in a manifold. The input air-line is essentially diverted to the one active syringe, with minimal additional dead-volume.

Of paramount importance was tying the new components in to the existing electronics and control architecture. The high level control scheme can be seen in Figure 4.10 below. The additional electrical components include: the Keyence system (transmitter, receiver, amplifier and communication module), the Nordson Ultimus V (and MAX3232 Transceiver chip to convert to and from TTL and RS-232), the three limit switches to determine the rotary state, and the four pressure multiplexing valves (driven through an external relay board).

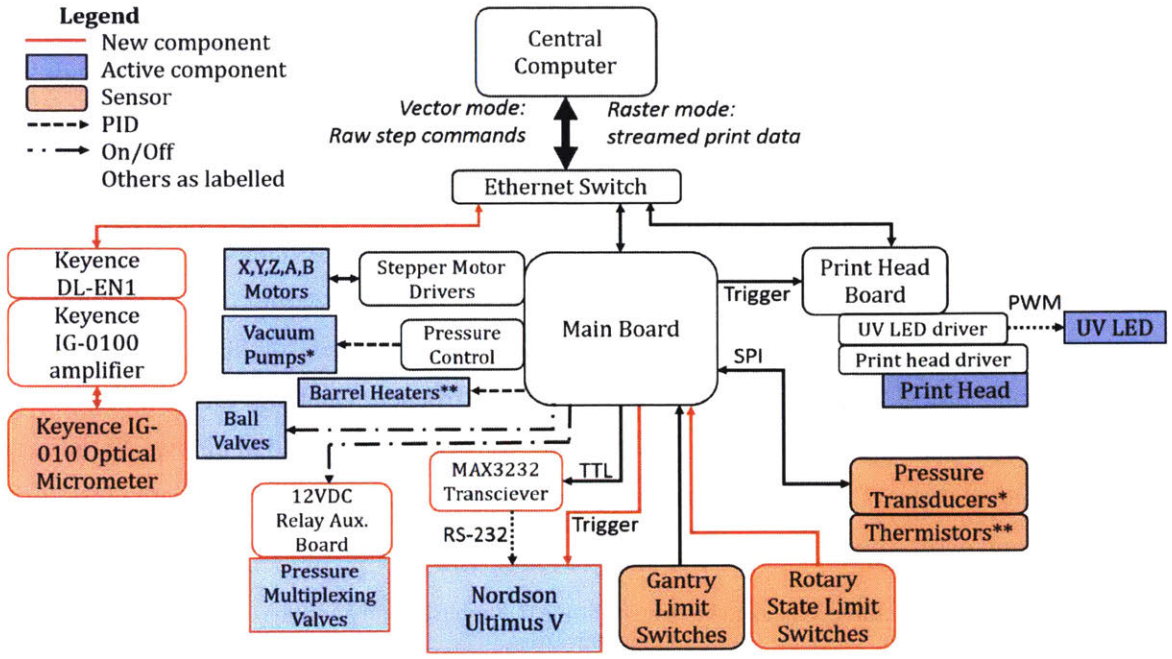

Figure 4.10: Simplified control and wiring schematic of the printer showing the newly added components (red outlines)

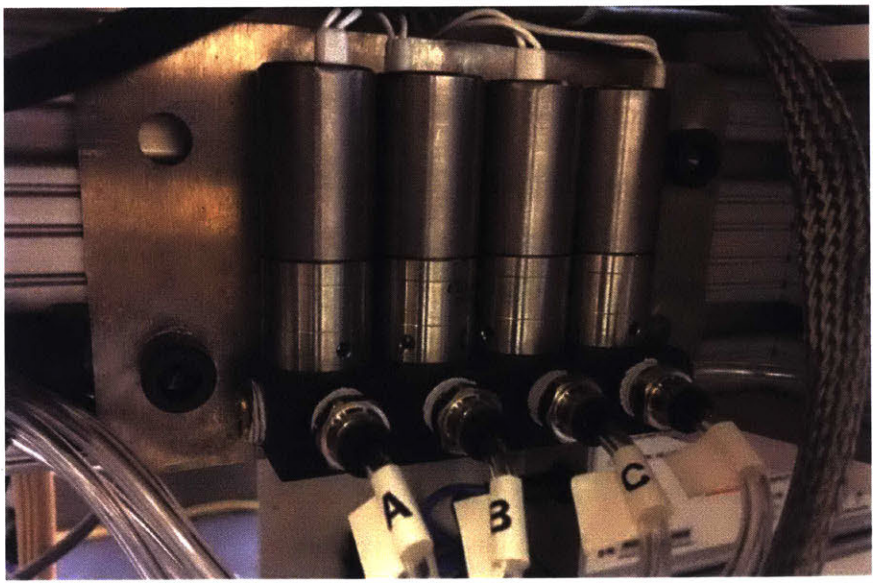

Figure 4.11: Photo of valve manifold assembly showing single inlet and multiple outlets

4.6 Registration

As both these deposition processes could be considered non-contact, their registration to a global origin becomes somewhat challenging. Because the inkjet process is very repeatable, all that is needed is to determine the spatial position of the nozzle. A solution using a single optical CCD micrometer (Keyence IG-010, with IG-1000 amplifier) was used to determine the XYZ coordinates.

By mounting the optical micrometer onto a precision rotary stage with magnetic hardstops (90 degrees apart), the sensor can read the position in the XY plane. As the syringes are mounted to a continuous Z axis, the Z position can be determined, without contact, by lowering the nozzle into the beam. The Z position for which the sensor first records the presence of an object is taken to be the tooltip Z offset. Due to the high repeatability of the gantry, the determination of the tooltip need only happen when a syringe is physically changed, i.e. only at the start of the print.

A drawing of the chosen coordinate systems on the rotating turret assembly can be seen in the figure below. Global zero is taken to be the center of the rotating platform to which the optical micrometer is mounted. By knowing a priori the offset between the measuring edge of the micrometer and global zero (X_0, Y_0), and the offset of the inkjet printing zero and the global zero, one can find the offset between the inkjet printing zero and the nozzle zero by using the two micrometer readings (X and Y).

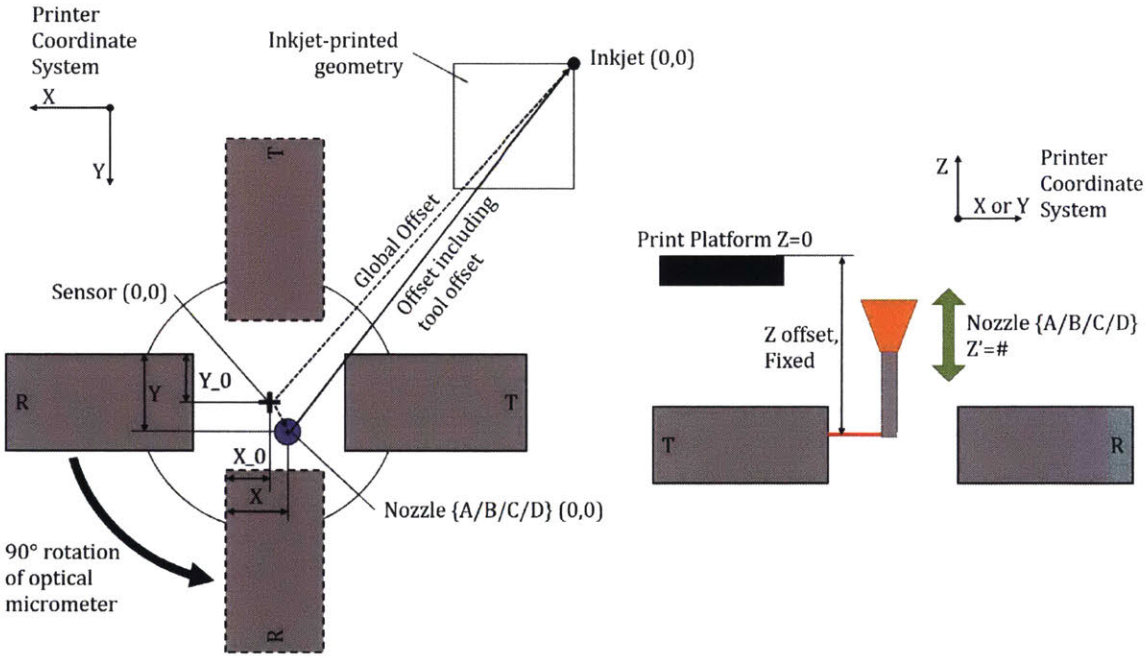

Figure 4.12: Schematic depiction of global coordinate system calibration system used to register inkjet and direct-write process in X, Y and Z (not to scale)

4.6.1 Registration Routine

An algorithm was developed to determine the location of the tooltip. In essence, after having moved the X' and Y axis to the prescribed homing location over top of the sensor array, the Z' axis is lowered until the sensor indicates the beam is broken (i.e. displays a reading). Due to some latency in the system and some mechanical backlash in the axis, an iterative search routine is employed to

better determine the correct Z' position at which the sensor is first tripped. The algorithm is very similar to a binary search procedure, and stops when the Z' motion is less than a prescribed error or 20 iterations have occurred. The user stores the Z_offset (the final Z' position from the iterative search process) along with the raw sensor value as X_offset in to a configuration file. The sensor array is then rotated on its precision rotary stage, and the new raw sensor value is recorded as Y_offset. This is registration routine is currently a semi-automated process, but could easily become fully-automated with the addition of a second CCD micrometer, eliminating the need for the manual rotary stage and allowing for the simultaneous determination of X, Y and Z offsets. The configuration file is used to compute both tool-specific offsets, akin to G10 command in G-code.

Chapter 5: Evaluation

As previously discussed, it is of paramount importance that the inkjet and direct-write processes are properly controlled such that there are no issues with unexpected interference or clearances between the printed geometries. Furthermore, many fluids are extremely sensitive to the offset distance between the substrate and the nozzle tip. Therefore, an investigation was done on the accuracy and repeatability of the direct-write system and the registration scheme.

5.1 Repeatability Measurements

The possible sources of error in the gantry were investigated incrementally, or in isolation where possible, in order to assign an error to each component. Unless otherwise noted, the Keyence optical micrometer was used as the measurement device and a 21 gage nozzle was the target object. It is important that the sensor array is mounted squarely to the printer's axes. This was verified by moving a nozzle within the sensor beam in both the X and Y directions and ensuring there were no deviations as the nozzle moved in the direction perpendicular to the measuring direction.

5.1.1 Sensor Repeatability

First, it was necessary to measure the repeatability of the reported value from the sensor. The sensor was configured to Mode E: "Theoretical center", from the right edge of the sensor array. It should be noted that the published repeatability is 5μm with the transmitter and receiver installed at a distance of 100mm from one another. The effect of the Z' axis cannot be fully eliminated. The datasheets for the precision linear bearings specify 2μm running parallelism, however this will be amplified at the tool tip. To mitigate any gantry-related effects, the Z' axis was moved a very small increment (1mm) in and then out of the beam. A total of 10 trials were performed in both the X and Y measuring directions, and a maximum range of 2μm was observed. Therefore, it is concluded the sensor repeatability, as installed, is 2μm.

5.1.2 Z' Repeatability

The Z' axis was driven into a dial indicator with 2μm resolution. After 10 trials, the axis was determined to be repeatable to 2μm or better, while there was significant backlash (70μm). Going forward, a backlash compensation strategy is employed.

5.1.3 Repeatability of Z' Determination

To measure the repeatability in Z', a 21 gauge nozzle was lowered into the beam at a rate of 3mm/s. Using feedback from the sensor through the DL-EN1 TCP/IP communication module, and

employing the aforementioned binary-search routine, the Z' height at which the sensor changed from "no objet detected" to a reading was obtained. It should be noted that any random error present in the Z' axis linear bearing would be present, however this measurement should be relatively insensitive to these roll, pitch or yaw or XY translational errors. It also includes the repeatability of the Z' axis itself. A series of 10 trials was performed and a range of 4μm was observed.

5.1.4 Repeatability and Accuracy of the X' Axis

As this axis is driven by a stepper motor without feedback, both backlash and errors in the computed steps/mm value can lead to inaccuracies. The magnitude of the backlash was quantified by driving the X' axis from a center position with a nozzle tip lowered and breaking the Keyence sensor beam, to the right, back to center, taking a reading, and then to the left, then back to center, and taking another reading. This process was repeated 10 times, and a backlash of 20μm was observed, while the repeatability could be 2μm with backlash compensation strategies.

5.1.5 Repeatability of the Carousel

The next source of error in the serial chain would be the effect of the repeatability of the carousel, specifically that of the spring detent and, to a lesser extent, the ABEC-7 bearing. Due to the geometry, it was determined that the sensitive direction is the X position of the nozzle tip, so only this axis was measured. This is illustrated graphically in the figure below. By simple geometry, it can be shown that a lateral error of 0.001" in the detent seating will cause a 5μm error in the tooltip position within the sensor field, in the worst case syringe configuration.

Keyence sensor readings were taken after rotating CW then CCW in a fully-automated fashion (using the passive rotation arms) and then using Z' to drop the nozzle in to the sensor beam. The same procedure was repeated after rotating in the opposite order (CCW then CW). The results can be found in the table below.

This test includes all the previous sources of error, except for the sensor's rotary stage rotation as only the sensitive direction was measured here. Clearly, each directionality has a different mean value, which can be partially attributed to the backlash in the X' axis. This could be eliminated by going to closed-loop control on the X' axis with the addition of an encoder.

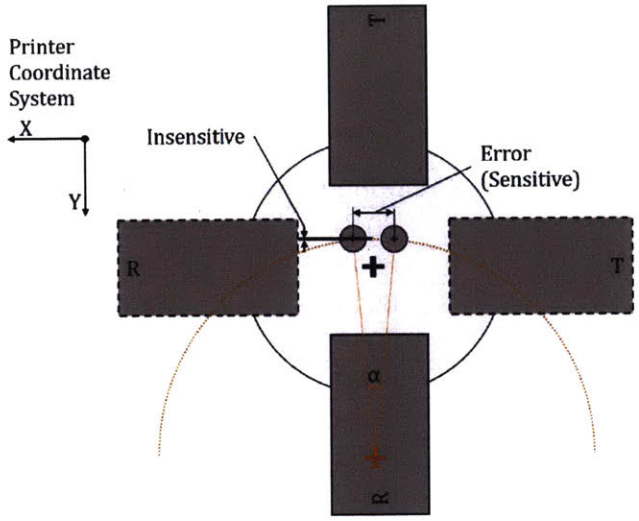

Figure 5.1: Sensitive direction of detent and carousel rotation (not to scale). Any angular error, α, about the carousel's main bearing leads to a (comparatively) large error in the X direction and a small error in the Y direction.

Table 5.1: Tooltip repeatability measurements under automated carousel rotation (both clockwise and counterclockwise)

Trial	CW then CCW (μm)	CCW then CW (μm)
1	4468	4465
2	4468	4465
3	4467	4463
4	4472	4462
5	4474	4463
6	4472	4460
7	4473	4459
8	4470	4458
9	4473	4459
Range	**7**	**7**
Average	**4461.6**	**4470.8**
Tot. Range	**16**	

5.1.6 Repeatability of Rotary Stage

The last source of error on the sensor that was investigated was the repeatability of the rotary stage to which it is mounted. The datasheet for the Thorlabs QRP02 specifies a repeatability of <15μRad. This leads to a negligible theoretical error at the sensor. To test this error, the rotary stage was moved manually between its hardstops while keeping the nozzle in the exact same location. The measurement was repeated 10 times and recorded at both the X and Y configurations, rotating the stage between the two configurations. There was a 13μm range on the reported values. This error can be solely attributed to the repeatability of the sensor itself, which is known, and the added error from the rotary stage. It was observed that different readings resulted from a change in pitch about the rotation axis, combined with potential deflection of the hardstops on the rotary stage. This error

can be entirely removed by adding in a second Keyence sensor to read in the other direction and removing the rotary stage altogether.

Table 5.2: Repeatability of sensor on rotary stage with a static tooltip

Trial	X reading (μm)	Y reading (μm)
1	6019	4402
2	6018	4401
3	6015	4401
4	6017	4400
5	6012	4395
6	6010	4396
7	6009	4401
8	6009	4395
9	6006	4397
10	6018	4389
Range	**13**	**13**

5.1.7 Repeatability Summary

The table below summarizes the results from the preceding discussion. As some effects could not be fully isolated, it is possible the summation of included effects does not equal an observed result.

Table 5.3: Repeatability measurements summary

Source of Error	Measured Range (μm)
(1) Sensor reading	2
(2) Z' axis	2
(3) Z' Determination	4
(4) X' axis	2 with 20 backlash
Carousel, sensitive direction (X), automated	7, 13 backlash
(5) Rotary stage for sensor	13
Y error*	**±1 + Y axis error**
X error*	**±8**
Z error*	**±2**

*Excluding effect of rotary stage

5.2 Overall Calibration Routine versus Inkjet Printed Geometry

The final test of the calibration routine is the repeatability of the extruded with respect to inkjet printed geometry. After much trial and error, the distance between the Keyence sensor array center of rotation and the inkjet zero point was determined, as well as the Z offset between the optical micrometer beam and the print platform. A series of inkjetted crosses were printed on the platform,

after which a matching pattern was extruded on top. The syringe was re-calibrated after every deposition. The printed geometries were compared optically at the extremes of the build platform. A measured error of approximately 80μm was observed over the entire print bed. This can be improved by building a corrective map of the build volume.

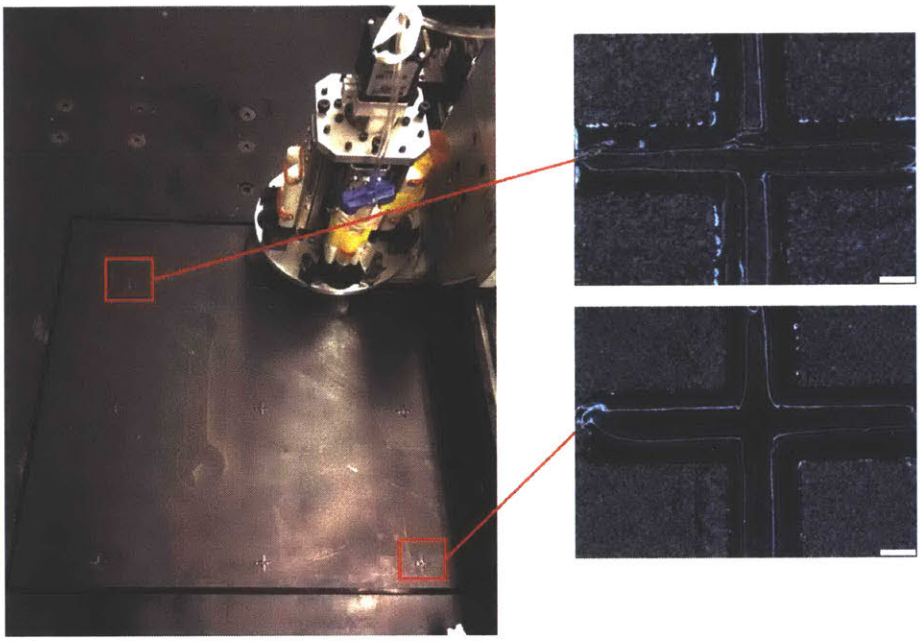

Figure 5.2: Process registration in XY plane showing nine printed crosses with inset optical microscopy of printed geometry at opposing corners. Scale bars 1mm.

5.3 Extrudate Cross-Section

It was determined that the most robust method of determining the extrudate cross-section is to carry out a series of replicates at the desired printing parameters, and to optically fit one of two models to the cross-section. This is because the extrudate can take on many shapes depending on fluid rheology, surface interactions and deposition parameters. For simplicity, a single road was studied here.

An experimental approach was taken to determining the printed extrudate cross-section. G-code was written to deposit lines at different printing parameters of interest (for example, different combinations of feed, pressure and Z-offset for a given nozzle diameter). A script in MATLAB was coded using a full-factorial approach to investigate the space. Here, 27 lines of 23wt% Pluronic F127 were printed following a 3^3 full factorial experiment. The three inputs were feed rate (1, 2, 3 mm/s), nozzle offset (.5, 0.75, 1mm), and pressure (15, 16.5 and 18psi). The extruded lines were deposited on top of a photopolymer substrate, after which additional photopolymer was cast to encapsulate it. The sample was then cleaved, mounted, and measured via optical microscope. Two different

geometric models were proposed to categorize the experimentally-observed cross-sections: a doubly truncated ellipse and a rectangle with filleted corners. These facilitate the transfer of information back to the CAD system in order to ensure proper geometric congruence. For ease of calculation, the formulas for their areas are also presented in the figure below. The formula for the double truncated ellipse was derived by simply subtracting the scaled chord areas for a circle of radius b from the ellipse. The upper truncation is typically created as a result of the nozzle acting as a doctor blade on the extruded geometry.

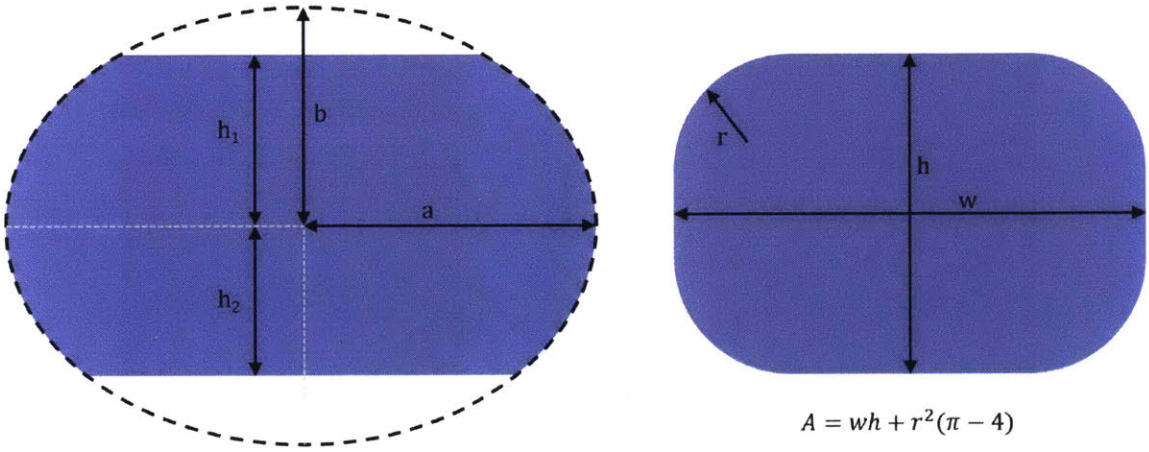

$$A = \frac{1}{2}ab\{2\pi - (\theta_1 - \sin(\theta_1)) - (\theta_2 - \sin(\theta_2))\}$$

$$\theta_1 = 2cos^{-1}\left(\frac{h_1}{b}\right)$$

$$\theta_2 = 2cos^{-1}\left(\frac{h_2}{b}\right)$$

$$A = wh + r^2(\pi - 4)$$

Figure 5.3: Two geometric models used to fit printed extrudate cross-sections – a truncated ellipse (left) and a rectangle with rounded corners (right). Formulas for areas are also presented.

A sample of images from the optical microscope fitting are shown below, along with the full table of all dimensions from the full factorial experiment. Here, the truncated ellipse fit was used for all cross-sections. These geometries can then be fed into the CAD model for improved accuracy. The under-extrusion in the first three trials can be attributed to the low offset and slow feed resulting in extruded material building up on the leading edge of the nozzle.

While the predictive flow rate models can be used to determine initial starting parameters, it is possible to observe extrusion problems such as flow instabilities or intermittent extrusion, and therefore this experimental fitting technique is recommended.

Table 5.4: Tabulated cross-section fit data

#	F (mm/s)	Z (mm)	P (psi)	Dimensions (mm)				A_CS (mm^2)	A_Exp (mm^2)	% Error
				a	b	h1	h2			
1	2	0.50	15.0	0.310	0.253	0.125	0.182	0.1762	0.45663	61%
2	2	0.50	16.5	0.618	0.396	0.380	0.296	0.7088	0.97023	27%
3	2	0.50	18.0	1.055	0.768	0.229	0.420	1.3157	1.76148	25%
4	2	1.00	15.0	0.386	0.405	0.224	0.405	0.4092	0.45663	10%
5	2	1.00	16.5	0.582	0.472	0.360	0.472	0.8053	0.97023	17%
6	2	1.00	18.0	1.055	0.568	0.348	0.568	1.6266	1.76148	8%
7	2	1.50	15.0	0.415	0.415	0.238	0.415	0.4566	0.45663	0%
8	2	1.50	16.5	0.702	0.520	0.306	0.520	0.9768	0.97023	-1%
9	2	1.50	18.0	0.711	0.721	0.549	0.601	1.438	1.76148	18%
10	3	0.50	15.0	0.334	0.320	0.224	0.320	0.3042	0.30442	0%
11	3	0.50	16.5	0.587	0.448	0.181	0.367	0.5826	0.64682	10%
12	3	0.50	18.0	0.969	0.786	0.105	0.539	1.1585	1.17432	1%
13	3	1.00	15.0	0.348	0.324	0.176	0.324	0.2933	0.30442	4%
14	3	1.00	16.5	0.492	0.454	0.334	0.454	0.6468	0.64682	0%
15	3	1.00	18.0	0.640	0.482	0.482	0.470	0.9668	1.17432	18%
16	3	1.50	15.0	0.334	0.348	0.210	0.348	0.3138	0.30442	-3%
17	3	1.50	16.5	0.539	0.396	0.305	0.396	0.6278	0.64682	3%
18	4	1.50	18.0	0.725	0.496	0.434	0.496	1.1003	0.88074	-25%
19	4	0.50	15.0	0.310	0.310	0.186	0.310	0.2589	0.22832	-13%
20	4	0.50	16.5	0.482	0.372	0.234	0.262	0.4394	0.48511	9%
21	4	0.50	18.0	0.788	0.544	0.186	0.425	0.8807	0.88074	0%
22	4	1.00	15.0	0.320	0.310	0.195	0.310	0.2718	0.22832	-19%
23	4	1.00	16.5	0.477	0.396	0.329	0.362	0.5604	0.48511	-16%
24	4	1.00	18.0	0.573	0.511	0.434	0.511	0.8883	0.88074	-1%
25	4	1.50	15.0	0.334	0.334	0.157	0.334	0.2761	0.22832	-21%
26	4	1.50	16.5	0.449	0.377	0.377	0.377	0.5318	0.48511	-10%
27	4	1.50	18.0	0.558	0.396	0.396	0.324	0.6628	0.88074	25%

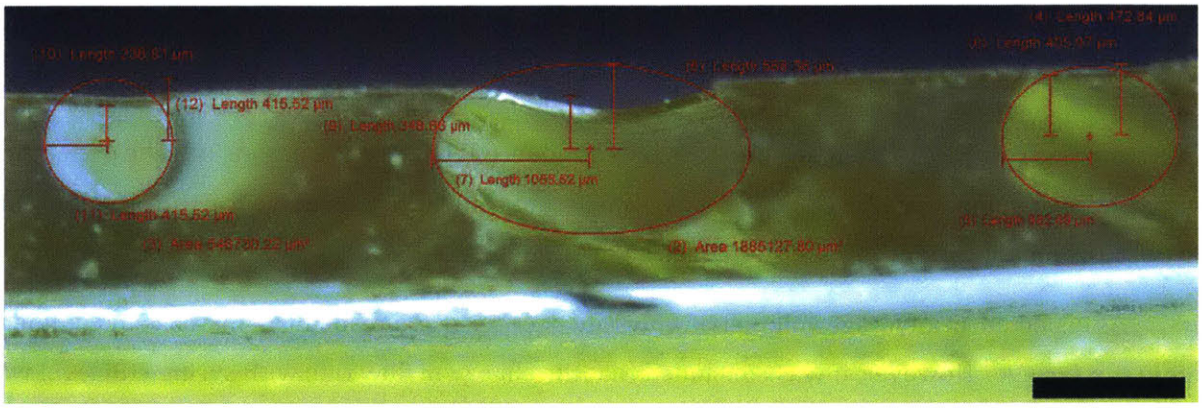

Figure 5.4: Microscope image of cleaved sample showing dimensions used for cross-section fitting of extruded roads. Scale bar 1mm.

5.4 Effect of Syringe Fill Volume on Flow Rate

An experiment was performed to quantify the possible influence of air compressibility on the steady-state flow rate. A solution of Pluronic F127 (24.5wt%) was loaded into two 10cc syringe barrels and degassed. One was filled to the manufacturer-recommended two thirds full, the other had approximately 10% filled. Fluid was dispensed at pre-programmed shot lengths onto pre-tared weigh paper through a 21 gauge nozzle. The weights were recorded, converted to an average volumetric flow rate using the density and dispensing time (10 seconds), and statistical inference on two samples techniques were used investigate the sample means and variances being equal. The data are shown in the table below.

Table 5.5: Study of syringe fill level on average volumetric flow rate

Trial	Average Volumetric Flow Rate (μL/s)	
	Full	10% Full
1	2.5333	2.2905
2	2.4381	2.3071
3	2.5238	2.4357
4	2.4857	2.3881
5	2.4286	2.4548
6	2.5333	2.4238
7	2.4381	2.4810
8	2.4571	2.4619
9	2.5143	2.4500
10	2.4667	2.4000
xbar	**2.4819**	**2.4093**
s	**0.0017**	**0.0042**

A t-test was performed under the assumption of unequal variances to determine the confidence at which one can conclude the population means are equal. The test p-value was 0.9955. A confidence interval on the difference in population means with α equal to 0.005 can be found below.

$$-0.0094\mu L/s \leq \mu_1 - \mu_2 \leq 0.1546\mu L/s \quad (5.1)$$

An F-test was performed to determine the confidence at which one can conclude the population variances are equal. The test p-value was 0.7930, indicating there is evidence to reject the null hypothesis (equal variances) at a confidence level of ~80%.

As expected, the average volumetric flow rate decreased as a result of an increase of volume of air in the syringe. However, it was concluded that the change in flow rate with syringe fill level was insignificant, especially considering the steady-state operation, long road lengths and smaller syringe

barrels normally used. Interestingly, the variance increased when the syringe is less full. Therefore, for more robust operation, one should print with near-full syringes. This agrees with the results presented in [26].

5.5 Flow Rate Prediction

The ability to predict the volumetric flow rate *a priori* would vastly facilitate working with fluids with different nozzle diameters and pressures. A simple validation of the predictive models presented in Chapter 2 are explored here.

5.5.1 Newtonian

Equation 2.5 was validated by dispensing N14 Viscosity Reference Fluid (Cannon Instrument Company) at different pressure settings and weighing the deposition. The diameter of the 26 gauge needle used was measured with an optical microscope, and the length with calipers. Viscosity data was taken from the supplier, and calibrated to the ambient lab temperature. Two replicates for each pressure setting was taken and the results are presented graphically below.

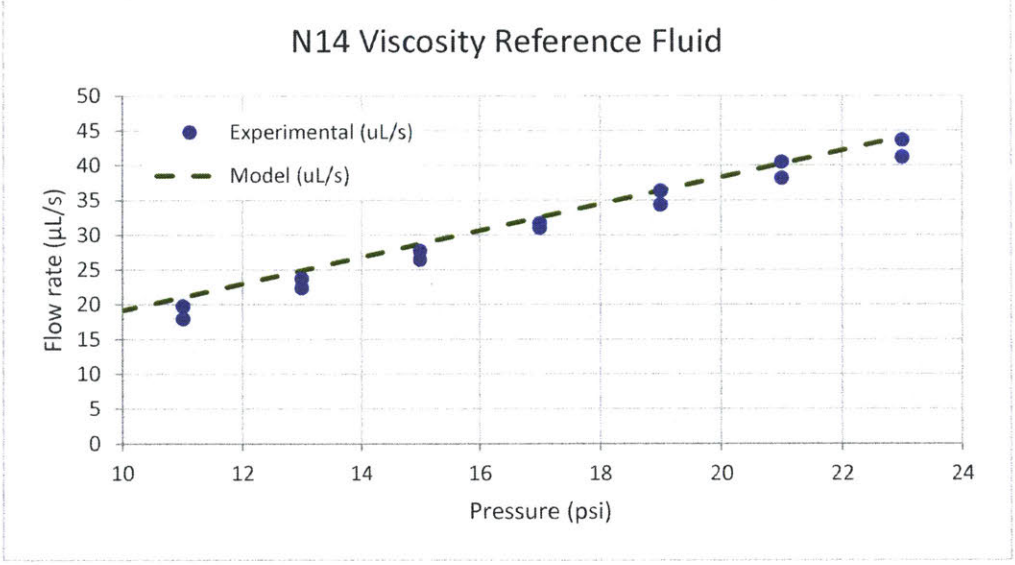

Figure 5.5: Flow rate vs. input pressure for N14 viscosity reference fluid through a 26 gauge nozzle. Experimental data points are plotted alongside the predictive Newtonian flow rate model.

The average error is 6%, with a standard deviation of 7%, indicating a good fit between the experimental results and theory.

5.5.2 Shear Thinning

Due to the challenges in determining the shear-stress versus shear-rate relationship for viscous fluids, as well as the extreme sensitivity of the flow rate on this relationship, proceeding

directly from rheometer data to a predicted cross-section is not recommended. Such complications include thixotropic effects, wall-slip and potential solvent evaporation. Instead, an experimental approach is suggested, where the fluid parameters are fit to experimental flow rate data. Such a fitting technique (least squares) was performed using carbon conductive grease (MG Chemicals 846) and is shown to work for a range of nozzle diameters. The fitted parameters for the power-law model are $K=406.6 Pa*s^n$ and $n=0.304$, versus $K=438.8 Pa*s^n$ and $n=0.0533$ from rotary viscometer data. The more complicated Herschel-Bulkley modes was also fitted but proved to almost identical in all cases, and so the simpler power-law model was used. It is probable that wall slip is present in this measurement as the exponent has been underestimated. The procedure, as above, involves extruding fluid at a given pressure for a known time and recording the extrudate mass, then transforming this to a volumetric flow rate using the fluid density. The dispensed fluid may be recycled to reduce waste. Such a process allows for the programmer to extrapolate the required pressure to achieve a desired flow rate with an arbitrary-sized nozzle. Ideally, one operates within the range of shear rates chosen in the experiment.

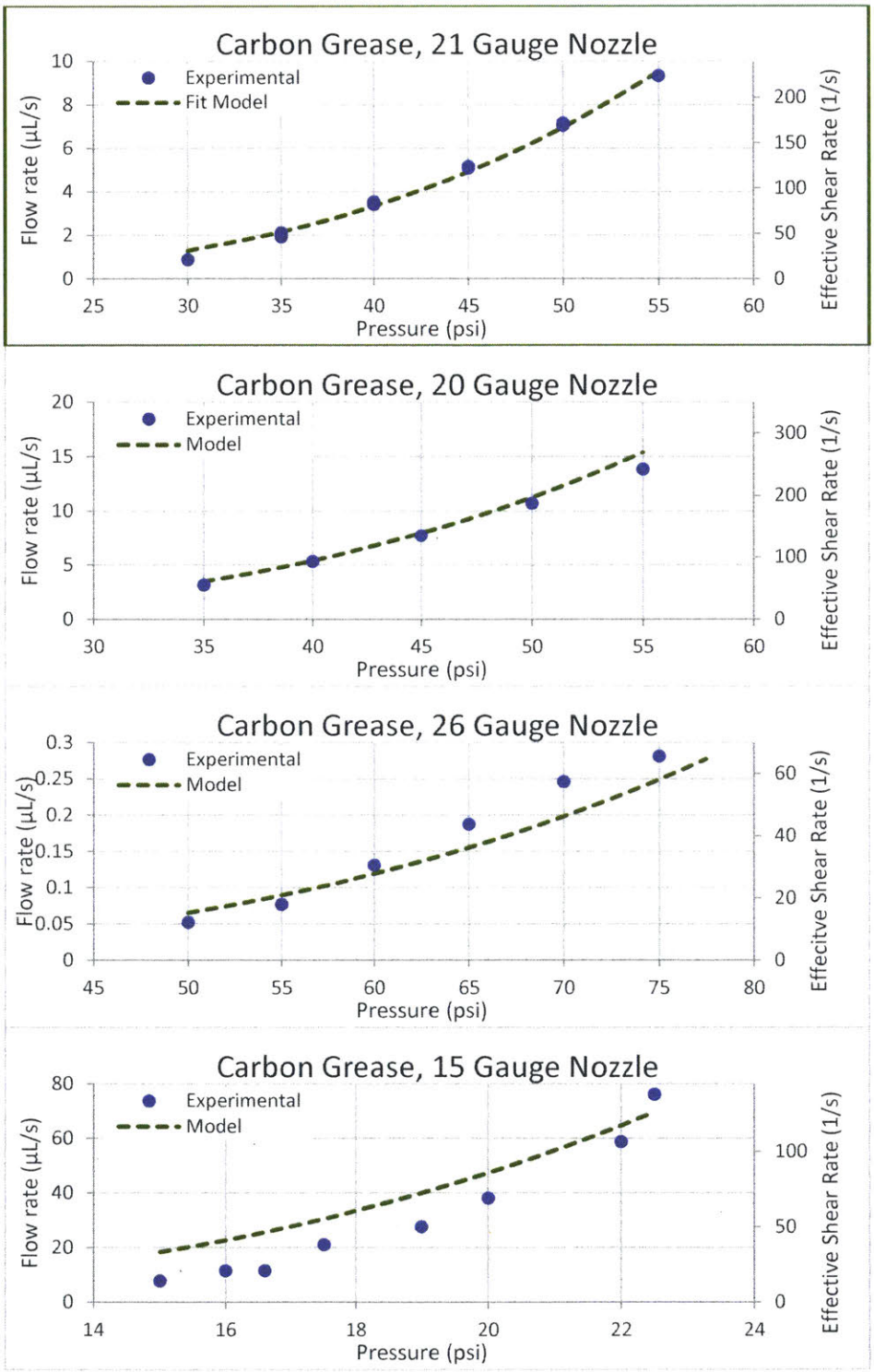

Figure 5.6: Experimental validation of power-law model (fitted to the 21 gauge data) for volumetric flow rate of carbon grease versus pressure over a range of nozzle sizes (21, 20, 26, 15 gauge). The corresponding effective shear rate is shown on the secondary axis.

(this page intentionally left blank)

Chapter 6: Applications

This section gives a preliminary outlook on the types of parts which might be fabricated with this system. The focus here realizing functionality using materials which cannot be inkjet printed.

6.1 Printed Microfluidics

There has been a large demand for quickly customizable microfluidic chips. Typical lithographic processes, while ubiquitous, are slow and constrained to largely planar structures. Major concerns for microfluidic systems often include channel dimensional fidelity, the ability to print 3D channels, and biocompatibility [42]. More advanced designs are adding functionality onto the chips, such as externally actuated valves and pumps, self-actuating valves [43] and integral sensing elements.

A simple microfluidic valve was created to demonstrate the capabilities of the hybrid deposition process. First, a base structure of rigid photopolymer was printed. Then the extruder was used to deposit a fugitive organic ink, Pluronic F127, in the geometry of the inlet channel and central void. Pluronic F127 is a thermo-gelling triblock copolymer which undergoes a phase transition according to its loading [44]. In effect, this means it can be easily washed out using only cold water, which makes it favorable to use a fugitive ink.

On top, a layer of elastic photopolymer was inkjetted as the flexible membrane. This was followed by a rigid well, to which a slurry of iron filing in a cationic curing epoxy was extruded. After UV curing the epoxy and washing out the fugitive ink with cold water, an external magnetic field could be applied to transition the valve from normally open to the closed state. A labelled cross-section and a photograph of the printed part can be found below.

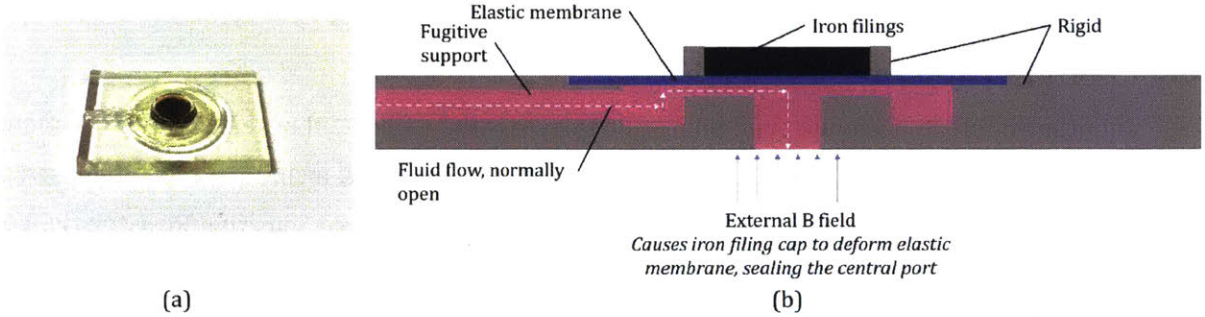

Figure 6.1: a) Photo fully-printed microfluidic valve b) Cross-section of device. Longest dimension is 30mm.

6.2 Fully-printed Tesla Turbine

A full-printed Tesla turbine was printed using extruded release layers. Tesla turbines run on compressed air and makes use of the boundary layer effect as opposed to conventional turbines which use fluid impinging on blades. The use of release layers made for a nominally zero-clearance conical bearing arrangement, constraining the disk blades both radially and axially. A brief description of the printing process and geometry follows.

Here, a highly loaded solution of graphite particles suspended in water with was dispensed into an inkjet printed well. Upon evaporating the water, a thin layer of graphite remains and is sufficient to make a clean interface between subsequently inkjet printed geometry. The design also makes use of a custom-formulated inkjettable water-soluble support. The upper bearing surface release layer was made by depositing a molybdenum disulfide grease, but could be redesigned to also use the graphite and water suspension.

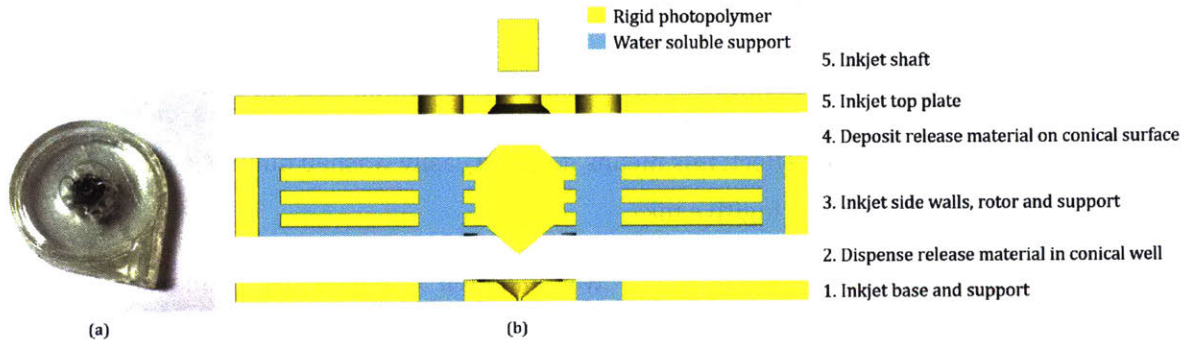

Figure 6.2: a) Photo of fully-printed Tesla turbine b) Cross-section of turbine showing printing steps. Diameter is 25mm.

This architecture has the potential to be expanded to an electromagnetic actuator as the geometry is very similar to a pancake motor. Such a motor typically has a rotor made from printed circuit boards and permanent magnets in the stator making it a DC commutated variety.

6.3 Flexible Pressure Sensor Array

Another interested avenue enabled by this system is the embedded of sensors into functional objects. Many sensing modalities of force or pressure sensors exist, including: capacitive, strain, piezoresistive and elastoresistive. Belong to the latter category, a Force Sensitive Resistor (FSR) is developed here. Through a multiplexed architecture, it is possible to create a dense array of pressure pixels (referred to as tactels) with few conductors [45]. Many objects can benefit from additional sensors. A specific use-case can be found in robotics, where often times a robot may be controlled quasi-open loop, using only vision. The addition of a dense array of pressure sensitive pixels on the

surface of end effectors will be useful in closing the loop and adding additional closed loop control, and is an active area of research [46].

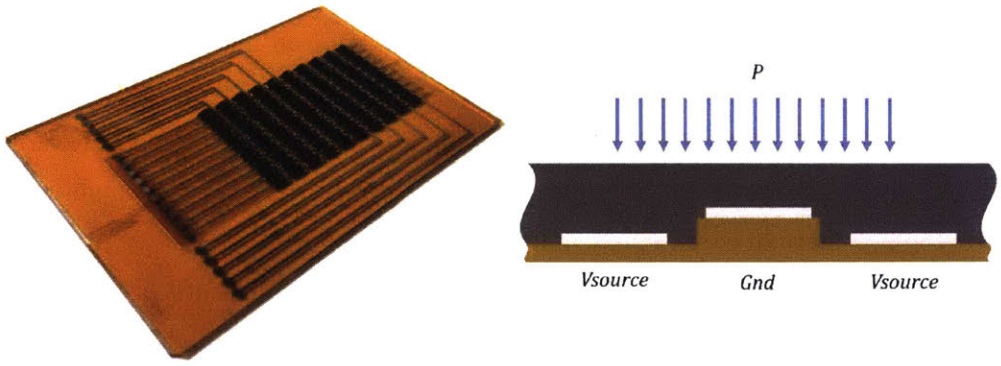

Figure 6.3: a) Photo of fully-printed device b) Cross-section of single tactel showing electrodes (not to scale)

6.3.1 Architecture and Fabrication Overview

This sensor was completed using two inkjet materials (a custom formulation of UV curable epoxy and a commercial nanoparticle silver ink (ANP Co., DGP 40LT-15C)) and one extruded material (a custom PDMS blend). The architecture can be described as a single-sided (lateral junction) array type sensor. An exploded view of the assembly is presented below, with a description for how the deposition occurs.

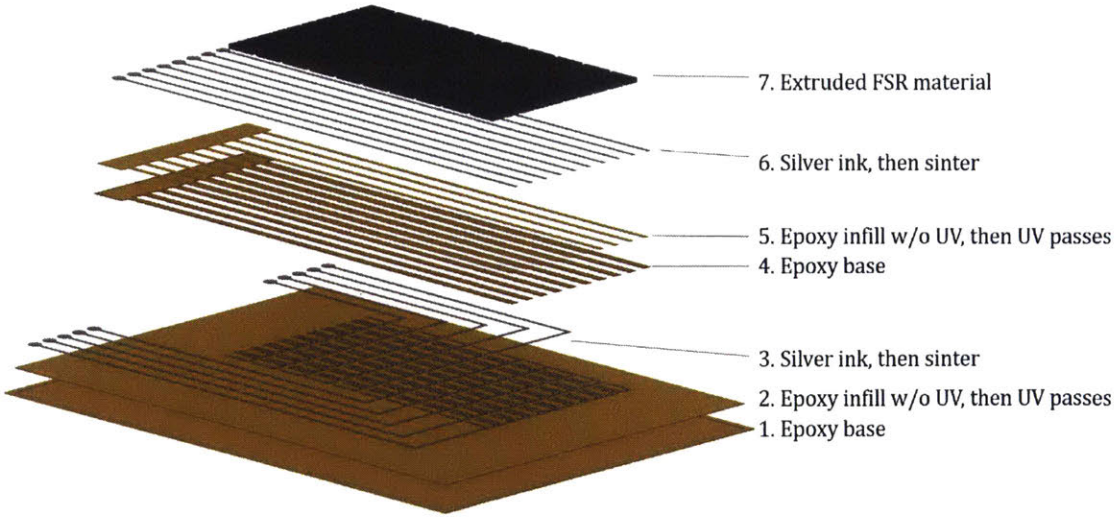

Figure 6.4: Exploded view of pressure sensor annotated with printing steps

Flexibility is achieved by keeping the epoxy layers very thin (approximately 250μm). Alternatively, the device can be printed on a conventional substrate suck as polyimide. The pattern fidelity of the commercial silver is greatly improved when the surface is smooth and also heated. To

this end, a substrate heater was used during the silver printing steps, set to approximately 120°C. This is high enough to flash off some of the solvent immediately upon heating the surface. Also, an unusual printing technique was used to make glass-like surfaces of the photopolymer. This techniques exploits the self-levelling of the thin fluids to mask an imperfections from the layers below. First, a well is printed with curing each pass, as usual. Then, without the UV light, the well is filled or over-filled with the same fluid. After allowing it to settle (for minutes, better results for if left for hours), a final series of UV-only passes cures the material. Surface roughness data was obtained on the pre-thermal cured epoxy material using a contact profilometer with a 2μm tip. A representative trace in the printing direction and across the printing direction are displayed. Clearly, longer range trends may exist (on the order of mm), but shorter wavelength features appear to be ±2μm. By comparison, a cross-section along a sintered silver line reveals an average height of approximately 3μm.

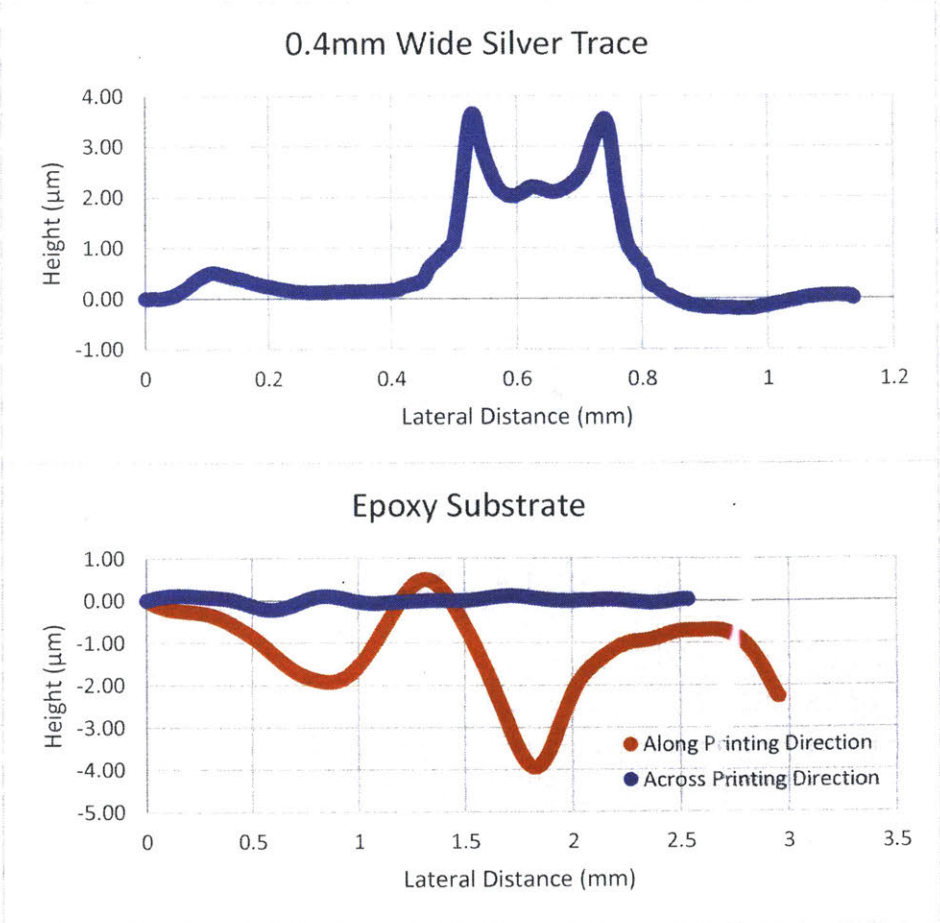

Figure 6.5: Profilometry data of epoxy substrate made using 'lake printing' technique and silver traces

The commercial silver requires a sintering temperature of 150°C for approximately 20 minutes to burn off the ligands (which are used to keep the nanoparticles in suspension). Also, the custom epoxy requires a thermal post-treatment for a full cure. While PDMS does cure at room temperature in 48 hours, it can be cured in minutes at 150°C. While thermal processing during fabrication was performed using an oven, in-situ curing of each of the constituents was independently verified using a ceramic infrared (IR) heater (Omega R-78613). Surface temperatures of approximately 600°C were observed with a non-contact thermometer.

As with any array type sensor, one must be conscious of the alternate current paths. Here, a through-thickness type device is presented as opposed to a lateral junction, however both architectures have the same potential issue. Essentially, there are multiple parasitic paths, which will negatively impact the gauge factor. This effect can be mitigated with smart measuring techniques involving selectively grounding the other electrodes and using a series of operational amplifiers [47]. Additionally, grounding techniques for the unused electrodes can lead to better sensor isolation [48]. Another possible current path, not pictured, is between parallel electrodes through the FSR material. This effect is eliminated by using discrete sensing elements at the junctions as opposed to a continuous sheet. Yet another solution is to employ an FSR with an extremely high gauge factor to mask the effect.

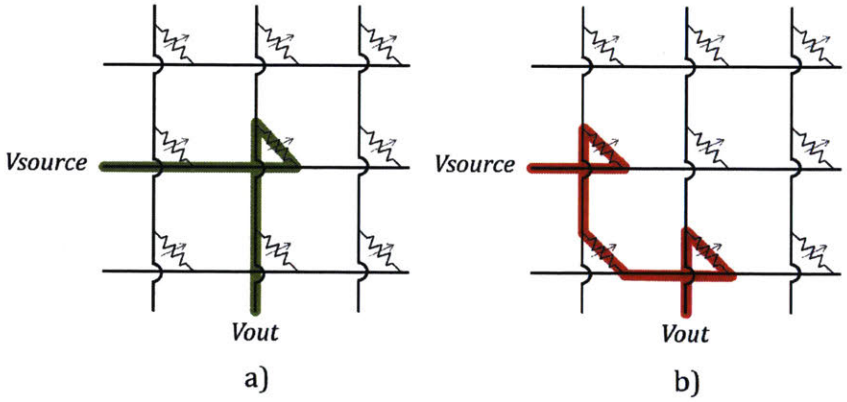

Figure 6.6: Schematic of a 3x3 sensing array. a) Shows the desirable current path through the center resistor b) Shows one of several possible alternate current paths which pass through nearby resistors and junctions

6.3.2 Ink Development

It is known that polymers loaded with a high percentage of carbon black or graphite or other conductive micro or nanoparticles can function as a variable resistor. An application of pressure on the material causes addition conducting polymers to come into contact and therefore reduces the resistance [49], or a negative pressure coefficient. These changes in resistance occur because the composite (polymer and conductive filler) exists near the percolation threshold and adjacent

particles come into contact. Another mechanism which might also be at play is quantum tunneling effects between neighboring particles, which can lead to very high sensitivity (gauge factors, R/R_0, as high as 400). The opposite response (a positive pressure coefficient) is possible if the particles have a high aspect ratio: the compressive strain leads to the separation of adjacent particles in the polymeric matrix [50] .

Here, a system comprising PDMS prepolymer (Dow Corning, Sylgard 184) loaded with 25.5wt% hydrophobic graphite nanopowder (400nm-1.2μm, US Research Nanomaterials) and 14wt% copper powder (<75μm, Sigma Aldrich). The curing agent is then added in a ratio of 1.67:10 to the prepolymer and the mixture is degassed. The formulation was tuned to give a baseline resistance in the mid kΩ range. Lower loadings resulted in a non-monotonic response to increasing force. It is suspecting that this is the result of two competing mechanisms. First, the change in cross-sectional area tends to increase the resistance, until the conductive particles start packing densely enough to start decreasing the resistance. The behavior is also heavily dependent on the electrode spacing. PDMS is a two part chemistry, capable of curing at room temperature. Its pot life, defined as the time at which the viscosity doubles, is approximately 90 minutes, which is sufficiently long to extrude the necessary features.

As the PDMS composite does not exhibit a yield stress, it must be printed into wells (or rapidly cured). This property was exploited to aid in creating a level-surface from the initially non-uniform printed roads.

6.3.3 Characterization

The response of the single tactel was characterized as a function of the applied load and time. A precision source meter (Keithley 2611B) was used to measure the resistance under application of 0.1V on a custom interdigitated substrate with a total of three 3mm long fingers with a 0.3mm gap. A digital force gauge (Wagner Instruments FDX 25) was used to modulate the pressure in the useful range for hand gripping strength. An initial preload was applied to mitigate the effects of changing contact resistance. It can clearly be seen that the tactel tracks the applied pressure although it does have some hysteresis. The annotated response curve can be seen below; the corresponding gauge factor for this range of pressure is approximately 2.8.

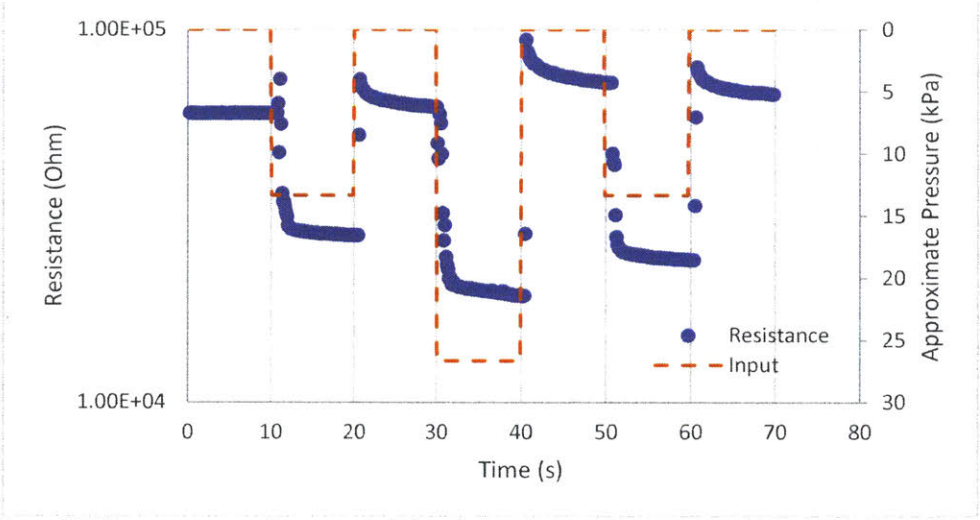

Figure 6.7: Response curve for one tactel, showing resistance versus approximate pressure and time.

(this page intentionally left blank)

Chapter 7: Summary and Future Work

In conclusion, a hybrid additive manufacturing machine combining photopolymer inkjet and time-pressure dispensing was conceptualized, designed and tested and several preliminary applications were demonstrated. A prototype system was created for preliminary integration work and for experimentation with the process. The second generation device introduced added features and automation: a multiplexed output and a carousel assembly such that four different materials may be extruded during the print, in addition to an optical micrometer for tooltip registration. Experimental results of the registration routine and gantry were performed to quantify the repeatability of the system. Under open-loop control, the nozzle tip position could be registered in the XY plane to ±8μm and the Z direction to ±2μm, which exceeds specifications and the conservative error budget. The dispensing process was also tested to be sufficiently repeatable and controllable. The increase in the available materials and printing techniques has expanded the engineer's toolbox. This freedom allowed for the development of a fully printed pressure sensor array and a microfluidic valve which would not have been possible using any single form of AM.

An open area of research is the development of software tools which will allow designers to exploit the added functionality of the system, and the many available printing modes. Another avenue for improvement would be to close the loop on the direct-write process. Specifically, by incorporating machine vision, such as Optical Coherence Tomography, to determine the exact shape of the extruded road and using software to dynamically alter the subsequent voxel grid which it to be inkjet printed (while maintaining design intent). Further hardware improvements would include the addition of a UV ring light around the nozzle for the instant curing of UV-curable inks and an infrared heater for rapid, in-situ evaporation of solvents and, potentially, sintering of nanoparticle inks.

Regarding the pressure sensor, further optimization can be done on the force sensitive resistive material itself for higher sensitivity and less hysteresis. Additionally, the appropriate drive circuitry and data logging software should be developed to capture the full 10x10 array, and the device can be made to conform to a particular geometry of interest, such as a robotic gripper.

Another promising avenue on the process side would be the exploration of reactive chemistries. Such approaches would take advantage of the multi-material, voxel-level control offered by inkjet while simultaneously working with extruded fluids which cannot be jetted from a conventional inkjet head.

The flexibility of the hardware that was developed along with the process characterization will enable many future projects and applications.

References

[1] C. Beyer, "Strategic Implications of Current Trends in Additive Manufacturing," *J. Manuf. Sci. Eng.*, vol. 136, no. 6, p. 64701, 2014.

[2] E. Sachs, M. Cima, P. Williams, D. Brancazio, and J. Cornie, "Three Dimensional Printing: Rapid Tooling and Prototypes Directly from a CAD Model," *J. Eng. Ind.*, vol. 114, no. November 1992, pp. 481–488, 1992.

[3] I. Gibson, D. W. Rosen, and B. Stucker, *Additive Manufacturing Technologies: Rapid Prototyping to Direct Digital Manufacturing*, vol. 54. 2009.

[4] E. MacDonald and R. Wicker, "Multiprocess 3D printing for increasing component functionality," *Science (80-.).*, vol. 353, no. 6307, p. aaf2093-aaf2093, 2016.

[5] M. Vaezi, S. Chianrabutra, B. Mellor, and S. Yang, "Multiple material additive manufacturing – Part 1: a review," *Virtual Phys. Prototyp.*, vol. 8, no. 1, pp. 19–50, 2013.

[6] Rize3D, *How Rize ADP 3D Printing Works*. 2016.

[7] E. Giller, "Process For Fabrication of Three Dimensional Objects," US 9,277,366 B2, 2016.

[8] S. Ready, F. Endicott, G. L. Whiting, T. N. Ng, E. M. Chow, and J. Lu, "3D Printed Electronics," *2013 Int. Conf. Digit. Print. Technol.*, pp. 9–12, 2013.

[9] S. Ready, G. Whiting, and T. N. Ng, "Multi-material 3D printing," *Int. Conf. Digit. Print. Technol.*, vol. 2014–Janua, pp. 120–123, 2014.

[10] MGI, "CeraPrinter F-Serie."

[11] M. Vlasea, Y. Shanjani, A. Bothe, R. Kandel, and E. Toyserkani, "A combined additive manufacturing and micro-syringe deposition technique for realization of bio-ceramic structures with micro-scale channels," *Int. J. Adv. Manuf. Technol.*, vol. 68, no. 9–12, pp. 2261–2269, 2013.

[12] C. Tech, "About Collider," 2017. [Online]. Available: http://www.collidertech.com/about/. [Accessed: 01-Jan-2017].

[13] R. R. Ma, J. T. Belter, and A. M. Dollar, "Hybrid Deposition Manufacturing: Design Strategies for Multimaterial Mechanisms Via Three-Dimensional Printing and Material Deposition," *J. Mech. Robot.*, vol. 7, no. 2, p. 21002, 2015.

[14] A. J. Lopes, E. MacDonald, and R. B. Wicker, "Integrating stereolithography and direct print technologies for 3D structural electronics fabrication," *Rapid Prototyp. J.*, vol. 18, no. 2, pp. 129–143, 2012.

[15] J. A. Paulsen, M. Renn, K. Christenson, and R. Plourde, "Printing conformal electronics on 3D structures with aerosol jet technology," *FIIW 2012 - 2012 Futur. Instrum. Int. Work. Proc.*, pp. 47–50, 2012.

[16] E. Malone and H. Lipson, "Freeform Fabrication of Electroactive Polymer Actuators and Electromechanical Devices," *Thin Film.*, no. Table 1, pp. 697–708, 2004.

[17] E. Malone and H. Lipson, "Multi-material freeform fabrication of active systems," *Esda'08*, pp. 1–

9, 2008.

[18] J. Lan, "Design and Fabrication of a Modular Multi-Material 3D Printer," Massachusetts Institute of Technology, 2013.

[19] J. E. Ramos-Maltés, "MultiFab : A Multi-Material 3D Printing Platform," Massachusetts Insitute of Technology, 2014.

[20] J. G. Kwan, "Design of Electronics for a High-resolution, Multi-Material, and Modular 3D Printer," Massachusetts Institute of Technology, 2013.

[21] N. Reis and B. Derby, "Ink Jet Deposition of Ceramic Suspensions: Modelling and Experiments of Droplet Formation," *Mater. Res.*, vol. 625, pp. 117–122, 2000.

[22] B. Derby, "Inkjet Printing of Functional and Structural Materials: Fluid Property Requirements, Feature Stability, and Resolution," *Annu. Rev. Mater. Res.*, vol. 40, no. 1, pp. 395–414, 2010.

[23] J. H. Lee, R. K. Prud'homme, and I. A. Aksay, "Cure depth in photopolymerization: Experiments and theory," *J. Mater. Res.*, vol. 16, no. 12, pp. 3536–3544, 2001.

[24] J. Kai, "Modeling of Positive-Displacement Dispensing Process," 2008.

[25] EnvisionTEC, "The 3D-Bioplotter Family," 2017. [Online]. Available: https://envisiontec.com/3d-printers/3d-bioplotter/.

[26] Y. X. Zhao and X. Du Chen, "Model-based robust design for time-pressure fluid dispensing using surrogate modeling," *Int. J. Adv. Manuf. Technol.*, vol. 55, no. 5–8, pp. 433–446, 2011.

[27] P. Calvert, R. Crockett, J. Lombardi, J. O. Kelly, and K. Stuffle, "Extrusion methods for solid freeform fabrication," pp. 50–55.

[28] R. Suntornnond, E. Y. S. Tan, J. An, and C. K. Chua, "A Mathematical Model on the Resolution of Extrusion Bioprinting for the Development of New Bioinks," *Materials (Basel).*, vol. 9, no. 9, 2016.

[29] M. Vlasea and E. Toyserkani, "Experimental characterization and numerical modeling of a micro-syringe deposition system for dispensing sacrificial photopolymers on particulate ceramic substrates," *J. Mater. Process. Technol.*, vol. 213, no. 11, pp. 1970–1977, 2013.

[30] R. S. Crockett and P. D. Calvert, "The Liquid-to-Solid Transition in Stereodeposition Techniques," *Solid Free. Fabr. Symp.*, pp. 257–264, 1996.

[31] B. G. Compton and J. A. Lewis, "3D-printing of lightweight cellular composites," *Adv. Mater.*, vol. 26, no. 34, pp. 5930–5935, 2014.

[32] D. B. Kolesky, R. L. Truby, A. S. Gladman, T. A. Busbee, K. A. Homan, and J. A. Lewis, "3D bioprinting of vascularized, heterogeneous cell-laden tissue constructs," *Adv. Mater.*, vol. 26, no. 19, pp. 3124–3130, 2014.

[33] J. P. Swensen, L. U. Odhner, B. Araki, and A. M. Dollar, "Printing Three-Dimensional Electrical Traces in Additive Manufactured Parts for Injection of Low Melting Temperature Metals," *J. Mech. Robot.*, vol. 7, no. 2, p. 21004, 2015.

[34] J. C. Conrad, S. R. Ferreira, J. Yoshikawa, R. F. Shepherd, B. Y. Ahn, and J. A. Lewis, "Designing colloidal suspensions for directed materials assembly," *Curr. Opin. Colloid Interface Sci.*, vol. 16, no. 1, pp. 71–79, 2011.

[35] R. S. Brodkey, *The Phenomena of Fluid Motions*. Dover Publications, 1995.

[36] A. Allmendinger, S. Fischer, J. Huwyler, H. C. Mahler, E. Schwarb, I. E. Zarraga, and R. Mueller, "Rheological characterization and injection forces of concentrated protein formulations: An alternative predictive model for non-Newtonian solutions," *Eur. J. Pharm. Biopharm.*, vol. 87, no. 2, pp. 318–328, 2014.

[37] H. X. Li, J. Liu, C. P. Chen, and H. Deng, "A simple model-based approach for fluid dispensing analysis and control," *IEEE/ASME Trans. Mechatronics*, vol. 12, no. 4, pp. 491–503, 2007.

[38] N. Zhou, C. Liu, J. A. Lewis, and D. Ham, "Gigahertz Electromagnetic Structures via Direct Ink Writing for Radio-Frequency Oscillator and Transmitter Applications," *Adv. Mater.*, p. 1605198, 2017.

[39] Smoothie, "G codes," 2017. [Online]. Available: http://smoothieware.org/supported-g-codes.

[40] S. Awtar and J. M. Quint, "In-plane flexure-based clamp," *Precis. Eng.*, vol. 36, no. 4, pp. 658–667, 2012.

[41] A. H. Slocum, "error_budget_spreadsheet_2016 03 09.xlsx." 2016.

[42] N. Bhattacharjee, A. Urrios, S. Kang, and A. Folch, "The upcoming 3D-printing revolution in microfluidics," *Lab Chip*, vol. 16, no. 10, pp. 1720–1742, 2016.

[43] C. I. Rogers, K. Qaderi, A. T. Woolley, and G. P. Nordin, "3D printed microfluidic devices with integrated valves," *Biomicrofluidics*, vol. 9, no. 1, pp. 1–9, 2015.

[44] BASF, "Pluronic® F127 Surfactant Viscosity As a Function of Temperature & Concentration," 2006.

[45] I. Rosenberg and K. Perlin, "The UnMousePad," *ACM Trans. Graph.*, vol. 28, no. 3, p. 1, 2009.

[46] Z. Ji, H. Zhu, H. Liu, N. Liu, T. Chen, Z. Yang, and L. Sun, "The Design and Characterization of a Flexible Tactile Sensing Array for Robot Skin.," *Sensors (Basel).*, vol. 16, no. 12, 2016.

[47] F. Vidal-Verdú, M. J. Barquero, J. Castellanos-Ramos, R. Navas-González, J. A. Sánchez, J. Serón, and A. García-Cerezo, "A large area tactile sensor patch based on commercial force sensors," *Sensors*, vol. 11, no. 5, pp. 5489–5507, 2011.

[48] Y. J. Yang, M. Y. Cheng, S. C. Shih, X. H. Huang, C. M. Tsao, F. Y. Chang, and K. C. Fan, "An integrated flexible temperature and tactile sensing array using PI-copper films," *Int. J. Adv. Manuf. Technol.*, vol. 46, no. 9–12, pp. 945–956, 2010.

[49] K. C. Baby, U. Fikri, and N. Schwesinger, "Resistive characterization of soft conductive PDMS membranes for sensor applications," *SAS 2016 - Sensors Appl. Symp. Proc.*, pp. 344–349, 2016.

[50] S. Stassi, V. Cauda, G. Canavese, and C. F. Pirri, "Flexible Tactile Sensing Based on Piezoresistive Composites: A Review," *Sensors*, pp. 5296–5332, 2014.